

ADJOINT-BASED OPTIMIZATION AND INVERSE DESIGN OF PHOTONIC  
DEVICES

A DISSERTATION  
SUBMITTED TO THE DEPARTMENT OF APPLIED PHYSICS  
AND THE COMMITTEE ON GRADUATE STUDIES  
OF STANFORD UNIVERSITY  
IN PARTIAL FULFILLMENT OF THE REQUIREMENTS  
FOR THE DEGREE OF  
DOCTOR OF PHILOSOPHY

Tyler William Hughes  
June 2019

© Copyright by Tyler William Hughes 2019  
All Rights Reserved

I certify that I have read this dissertation and that, in my opinion, it is fully adequate in scope and quality as a dissertation for the degree of Doctor of Philosophy.

---

(Shanhui Fan) Principal Adviser

I certify that I have read this dissertation and that, in my opinion, it is fully adequate in scope and quality as a dissertation for the degree of Doctor of Philosophy.

---

(Robert L. Byer)

I certify that I have read this dissertation and that, in my opinion, it is fully adequate in scope and quality as a dissertation for the degree of Doctor of Philosophy.

---

(Olav Solgaard)

I certify that I have read this dissertation and that, in my opinion, it is fully adequate in scope and quality as a dissertation for the degree of Doctor of Philosophy.

---

(Mark Brongersma)

I certify that I have read this dissertation and that, in my opinion, it is fully adequate in scope and quality as a dissertation for the degree of Doctor of Philosophy.

---

(Amir Safavi-Naeini)

Approved for the Stanford University Committee on Graduate Studies

# Preface

This thesis tells you everything you need to know about...

# Acknowledgments

I would like to thank ...

# Contents

<b>Preface</b>	<b>iv</b>
<b>Acknowledgments</b>	<b>v</b>
<b>1 Introduction</b>	<b>1</b>
1.1 Photonics . . . . .	1
1.2 Designing of Photonic Devices . . . . .	2
1.2.1 Traditional Design Approach . . . . .	2
1.2.2 Inverse Design Approach . . . . .	2
1.3 Introduction to Adjoint Method . . . . .	3
1.4 Thesis Overview . . . . .	4
<b>2 Adjoint-Based Optimization of Accelerator on a Chip</b>	<b>5</b>
2.1 Dielectric Laser Acceleration . . . . .	5
2.2 Adjoint Method for Particle Accelerators . . . . .	7
2.3 Inverse design of Dielectric Laser Accelerator . . . . .	13
2.4 Optimization of acceleration factor . . . . .	18
2.5 Conclusions . . . . .	20
<b>3 Integrated Photonic Circuit for Accelerators on a Chip</b>	<b>22</b>
3.1 On-Chip Laser Coupling Device . . . . .	22
3.1.1 Input Coupling . . . . .	24
3.1.2 Waveguides . . . . .	25
3.1.3 Splitters . . . . .	25
3.1.4 Bends . . . . .	26
3.1.5 Phase Shifters . . . . .	28
3.1.6 DLA Structures . . . . .	29
3.1.7 Beam Loading and Longitudinal Wakes . . . . .	31
3.1.8 Heat Dissipation . . . . .	31

3.2	Parameter Study . . . . .	32
3.3	Automatic Controlled Power Delivery Systems . . . . .	32
3.3.1	Phase Control Mechanism . . . . .	32
3.3.2	Power Control Mechanism using Reconfigurable Circuit . . . . .	32
3.4	Experimental Efforts . . . . .	32
3.4.1	Waveguide Damage and Nonlinearity Measurements . . . . .	32
3.4.2	Demonstration of Waveguide-Coupled Acceleration . . . . .	32
<b>4</b>	<b>Training of Optical Neural Networks</b>	<b>33</b>
4.1	Introduction to Machine Learning . . . . .	34
4.1.1	Applications . . . . .	34
4.1.2	Hardware Demands . . . . .	34
4.2	Linear Nanophotonic Processors . . . . .	34
4.3	Optical Neural Networks . . . . .	34
4.3.1	Conventional Neural Network . . . . .	34
4.3.2	Optical Integration . . . . .	34
4.3.3	Training Protocols . . . . .	34
4.4	In Situ Backpropagation Training . . . . .	34
4.4.1	Derivation Using Adjoint Method . . . . .	34
4.4.2	Method for Measurement of Adjoint Gradient . . . . .	34
4.4.3	Numerical Demonstrations . . . . .	34
4.5	Electro-Optic Activation Functions . . . . .	34
4.5.1	Motivation . . . . .	34
4.5.2	Proposed Activation Function . . . . .	34
4.5.3	Scaling Laws . . . . .	34
4.5.4	Demonstration . . . . .	34
4.6	Wave-Based Analog Recurrent Neural Networks . . . . .	34
4.6.1	Wave Equation vs. Recurrent Neural Network . . . . .	34
4.6.2	Vowel Classification through Wave Propagation . . . . .	34
<b>5</b>	<b>Extension of Adjoint Method beyond Linear Time-Invariant Systems.</b>	<b>35</b>
5.1	Nonlinear Devices . . . . .	35
5.1.1	Generalization of Adjoint Method to Nonlinear Problems . . . . .	35
5.1.2	Inverse Design of Nonlinear Photonic Switches . . . . .	35
5.2	Active Devices . . . . .	35
5.2.1	Adjoint Sensitivity for Multi-Frequency FDFD Problems . . . . .	35
5.2.2	Inverse Design of Optical Isolators through Dynamic Modulation . . . . .	35
5.3	Adjoint for Time Domain . . . . .	35

5.3.1	Derivation . . . . .	35
5.3.2	Challenges . . . . .	35
5.4	Forward-mode Differentiation . . . . .	35
<b>6</b>	<b>Conclusion and Final Remarks</b>	<b>36</b>
<b>A</b>	<b>Something</b>	<b>37</b>



# List of Tables

2.1	Acceleration factor ( $f_A$ ) before and after maximization. . . . .	20
-----	--	----

# List of Figures

2.1	Diagram outlining the system setup for side-coupled DLA with an arbitrary dielectric structure $\epsilon(x, y)$ (green). A charged particle moves through the vacuum gap with speed $\beta c_0$ . The periodicity is set at $\beta\lambda$ where $\lambda$ is the central wavelength of the laser pulse. . . . .	6
2.2	Definition of the vector field, $\vec{\eta}$ , which defines the position of the electron in the frequency domain. The green regions represent domains where we will optimize the material properties using the adjoint method. The central gap is constrained to vacuum to allow passage of the electron beam. The red arrow signifies the driving laser. . . . .	9
2.3	Demonstration of adjoint method in calculating accelerator sensitivities. (a) The acceleration gradient ( $G$ ) of a square accelerator structure (inset) as a function of the square's relative permittivity. We express the acceleration gradient in its dimensionless form, normalized by the electric field amplitude of the incident plane wave ( $E_0$ ). The particle traverses along the dotted line with a velocity of $c_0$ ( $\beta = 1$ ) and a plane wave is incident from the bottom of the structure. (b) The sensitivity $\frac{dG}{d\epsilon}$ of the gradient with respect to changing the square relative permittivity for direct central difference (solid line) $\frac{dG}{d\epsilon} = \frac{G(\epsilon+\Delta\epsilon)-G(\epsilon-\Delta\epsilon)}{2\Delta\epsilon}$ and using the adjoint method (circles). The two calculations agree with excellent precision. The dotted line at $\frac{dG}{d\epsilon} = 0$ , corresponds to local minima and maxima of $G(\epsilon)$ above. . . . .	14
2.4	Optimization routine for DLA. . . . .	15

2.5	Demonstration of the structure optimization for $\beta = 0.5$ , laser wavelength $\lambda = 2\mu\text{m}$ , and a gap size of 400 nm. A plane wave is incident from the bottom in all cases. (a) Acceleration gradient as a function of iteration number for different maximum relative permittivity values, corresponding to those of Si, $\text{Si}_3\text{N}_4$ , and $\text{SiO}_2$ at the laser wavelength. The acceleration gradient is normalized by the electric field amplitude of the incident plane wave ( $E_0$ ). The optimizations converge after about five-hundred iterations. (b-d) Final structure permittivity distributions (white = vacuum, black = $\epsilon_m$ ) corresponding to the three curves in (a). Eight periods are shown, corresponding to four laser wavelengths. For each (b-d), design region widths on each side of the particle gap were given by 1, 2, and $4\mu\text{m}$ for Si, $\text{Si}_3\text{N}_4$ , and $\text{SiO}_2$ , respectively. . . .	16
2.6	Similarity between DLA structures designed using adjoint method (left) and those independently proposed using human intuition. . . . .	17
2.7	Demonstration of the final structures after optimization for (a) maximizing gradient only, (b) maximizing the acceleration factor. $\beta = 0.5$ , laser wavelength $\lambda = 2\mu\text{m}$ , gap size of 400 nm. $\epsilon_m = 2.1$ , corresponding to $\text{SiO}_2$ . In (a), the high gradients are achieved using reflective dielectric mirrors to confine and enhance the fields in the center region. In (b), these dielectric mirrors are removed and the pillar structures are augmented. The structure in (b) shows a 23% increase in the acceleration factor in the material region when compared to (a). . . . .	19
3.1	Two stages of the DLA laser coupling ‘tree-network’ structure. The electron beam travels along the z-axis through the center of this structure. The laser pulses are side coupled with optical power shown in red. Black regions define the on-chip waveguide network. Blue circles represent the optical phase shifters used to tune the phase of the laser pulse. This geometry serves to reproduce the pulse-front-tilt laser delivery system outlined in [?] in an integrated optics platform. . . . .	23
3.2	Waveguide geometries and corresponding horizontal electric field components [?]. (a-b) Strongly confined modes. (c-d) Weakly confined modes. (a) and (c) are SOI material platforms whereas (b) and (d) are $\text{Si}_3\text{N}_4/\text{SiO}_2$ materials. Waveguide core heights in (a-d) are given by 220, 400, 60, and 100 nm, respectively. Waveguide core widths are given by 0.78, 1.6, 2, and $4\mu\text{m}$ , respectively. . . . .	26
3.3	(a) Electric field amplitude for a strongly guiding SOI waveguide. (b) Electric field amplitude for a weakly guiding SOI waveguide. (c) Comparison of bending loss as a function of bend radius for the 4 waveguides from Fig. 3.2. . . . .	27

3.4	Idealized schematic of a feedback system for automatic phase control. A dedicated light extraction section is added to the accelerator. Light is radiated from the electron beam transversing the DLA structures and the frequency content and/or timing of the light is sent to a controller. The phase shifts of each waveguide are optimized with respect to either the frequency or the delay of the signal. . . . .	29
3.5	(a) A schematic of the waveguide to DLA connection. Silicon dual pillars of optimized radius of 981 nm and gap size of 400 nm are used. (b) The accelerating electric field during one time step. (c) Absolute value of the transverse magnetic field. (d) Absolute value of the acceleration gradient as a function of frequency, normalized by the peak electric field in the waveguide. A Lorentzian line shape is fit to the square of this plot. The square root of this fit is shown in red. Based on the Lorentzian fit, a Q-factor of $152 \pm 29$ was determined. As computed following the derivation in [38], but with the waveguide mode impedance and effective area in place of the plane wave values, this structure has a shunt impedance, $Z_S$ , of $449.1 \, \Omega$ over 3 periods and a $Z_S/Q$ value of $2.95 \, \Omega$ . . . . .	30

# Chapter 1

## Introduction

### 1.1 Photonics

The field of photonics is concerned with the study and manipulation of light. This endeavor has given rise to countless technologies of great practical and scientific interest. Most prominently, the use of light as an information carrier has enabled high speed and low loss communications through the use of optical fiber technologies [2]. Light is also used extensively for precise detection and measurement in scientific studies. For example, X-ray radiation is now used to observe femtosecond dynamics in chemical reactions [21], and laser interferometry was recently used to measure gravitational waves emitted from black hole mergers [27]. Apart from these, there are many applications of photonics with significant practical importance ranging from renewable energy [9, 48] to passive refrigeration [40, 17].

One of the most important achievements of photonics in the past few decades has been the development of *integrated* photonic devices [39]. In this paradigm, rather than constructing devices using macroscopic components, such as lenses and mirrors, they are created on the surface of a chip using techniques common to the semiconductor industry. Such an approach is appealing as it allows for compact, low cost, and highly functional devices that are also easier to integrate with existing electronic platforms based on composite metal on semiconductor (CMOS) technology [46]. The field of *silicon photonics* has especially generated much interest in recent years, in which photonic devices integrated on Silicon are employed in applications ranging from optical interconnects for fast data transfer between microchips to large scale integrated photonic circuits [18].

Here, we will primarily explore two emerging technologies based on integrated photonics, (1) Laser-driven particle accelerators on a chip, and (2) optical hardware for machine learning applications. The approach to laser-driven particle acceleration examined here is referred to as ‘dielectric laser acceleration’, in which charged particles are accelerated by the near field of a patterned dielectric structure driven by an external laser. As we will show, this technology may benefit greatly from

the use of integrated photonic platforms for its eventual practical applications. Integrated photonics is also a promising candidate for building hardware platforms specialized on machine learning tasks. As the transmission of an image through an optical lens passively performs a Fourier transform, reconfigurable integrated photonic devices are capable of performing arbitrary linear operations through pure transmission of optical signals through their domain. As machine learning models are often dominated by linear operations, this technology may provide a platform with higher processing speed, lower energy usage when compared to conventional digital electronics.

## 1.2 Designing of Photonic Devices

### 1.2.1 Traditional Design Approach

In any of these applications, the design of the photonic device is of critical importance. The typical approach to such a process is to use physical intuition to propose an initial structure. This structure may be parameterized by several *design variables*, such as geometric or material parameters. These parameters may then be optimized, using numerical simulation or experiment, until convergence on a functioning device that further satisfies fabrication constraints, such as minimum feature size, for example. As an example, if one is interested in designing a device that routes input light to different ports for different input wavelengths, one such approach would be to combine several wavelength filters into one device and tune their parameters until the functionality is achieved. Such an approach, while intuitive, has a number of potential drawbacks. First, it is dependent on the designer having significant physical intuition about the problem, which is not always available especially in novel applications. Second, the method of tuning parameters by hand is tedious and the time needed to complete such a task generally scales exponentially with the number of design variables. This fact means that the designer is practically limited to examining a small number of design variables or only a few select combinations. The use of few design variables further limits the designer to consider devices within a fixed parameterization. For example, if one were to design a device for tailored diffraction or transmission characteristics, he or she may decide to explore grating structures parameterized by tooth height, width, and duty cycle, while ignoring other possible designs.

### 1.2.2 Inverse Design Approach

*Inverse design* is a radically different approach that has become popularized in photonics within the past decade [31]. In this scheme, the overall performance of the device is defined mathematically through an *objective function*, which is then either maximized or minimized using computational and mathematical optimization techniques. This approach allows for automated design of photonic devices that are often more compact and higher performance than their traditionally designed alternatives. Furthermore, this approach allows one to search through a much larger parameter space,

typically on the order of thousands to millions of design variables, which allows the design algorithms to often find structures with complexities often extending beyond the intuition of the designer.

The use of inverse design has a long history in other fields, such as mechanics [45], aerodynamics [19], and heat transfer [34]. However, in the past decade, it has been applied successfully to many photonics problems. A few early examples include the use of inverse design to engineer wavelength splitters [36, 23], perfect 90 degree bends in dielectric waveguides [20], or the design of photonic crystals [6]. More recently, it was applied to engineer more exotic phenomena, such as the photonic crystal band structure [PhC band], nonlinear optical responses [28], and metamaterials [42]. For a thorough overview of the progress of inverse design in photonics at the time of publishing, we refer the reader to Ref. 31.

### 1.3 Introduction to Adjoint Method

As we will explore in detail, the ability to perform inverse design is largely enabled by the ability to efficiently search such a large parameter space. Typically, this is performed using *gradient-based optimization* techniques, which use local gradient information to iteratively progress through the design space. In design problems with several degrees of freedom, gradient-based methods typically converge on local minima much faster than more general optimization techniques such as particle swarm optimization [1] or genetic algorithms [47], which don't typically use local gradient information.

In problems constrained by physics described by linear systems or differential equations, the *adjoint method* is used to compute these gradients. The adjoint method allows one to compute gradients of the objective function with respect to each of the design parameters in a complexity that is (in practice) independent on the size of the design space. As such, it is the cornerstone of the inverse design works in photonics and other fields.

Here we give a brief introduction to the mathematics behind the adjoint method. Many engineering systems can be described by a linear system of equations  $A(\phi)\mathbf{x} = \mathbf{b}$ , where  $A$  is a sparse matrix that depends on a set of parameters describing the system,  $\phi$ . Solving this equation with source  $\mathbf{b}$  results in the solution  $\mathbf{x}$ , from which an objective function  $J = J(\mathbf{x})$  can be computed.

The optimization of this system corresponds to maximizing or minimizing  $J$  with respect to the set of parameters  $\phi$ . For this purpose, the adjoint method allows one to calculate the gradient of the objective function  $\nabla_{\phi} J$  for an arbitrary number of parameters. Crucially, this gradient may be obtained with the computational cost of solving only one additional linear system  $\hat{A}^T \bar{\mathbf{x}} = -\frac{\partial J}{\partial \mathbf{x}}^T$ , which is often called the 'adjoint' problem.

As we will show, this method may be readily applied to the inverse design of electromagnetic devices. In this case,  $A$  represents Maxwell's equations describing the device,  $\mathbf{x}$  are the electromagnetic fields, and  $\mathbf{b}$  is the electric current source driving the system.

## 1.4 Thesis Overview

Like inverse design, the adjoint method has been known in the applied math community for quite some time, and has been applied to numerous other fields. Its application to photonics is quite recent, but has had a significant impact. In this thesis, we will discuss the application of the adjoint method to new applications in photonics. We will also introduce extensions to the adjoint method, which allow it to be applied to new systems and implemented experimentally. The thesis is organized as follows. In Chapter 2, we will introduce the mathematical details behind adjoint-based optimization. To give a concrete example, we will focus on its application to laser-driven particle accelerators on a chip. To continue this discussion, in Chapter 3, we will discuss the scaling of laser-driven particle accelerators to longer length scales using photonic integrated circuits. This discussion will motivate the need to use inverse design for new components, and we will discuss efforts to use such techniques to build these systems experimentally. In Chapter 4, we will discuss optical hardware platforms for machine learning applications. The adjoint method will be explored in the context of training an optical neural network, and we will show that its implementation corresponds to the backpropagation algorithm of conventional neural networks. A novel method for experimentally measuring the gradients obtained through the adjoint method will be introduced in the context of machine learning hardware and we will also discuss our exploration of nonlinear optical activation functions and time-domain machine learning processing using wave physics. In Chapter 5, we will explore the extension of the adjoint method to new scenarios in photonics, namely nonlinear and periodically modulated systems. We will conclude in Chapter 6.



## Chapter 2

# Adjoint-Based Optimization of Accelerator on a Chip

### 2.1 Dielectric Laser Acceleration

In the public sphere, particle accelerators most commonly conjure images of giant particle colliders, such as the Large Hadron Collider. However, most particle accelerators are used in other applications, such as radiotherapy, X-ray generation, and ion implantation for semiconductor device fabrication [14]. Conventional radio-frequency (RF) accelerators use a metal or superconducting cavity, driven with microwave radiation, to provide sustained acceleration to charged particles traversing the structure. However, the available acceleration per length is fundamentally limited by the material breakdown and damage of the cavity. Therefore, for an accelerator driven at its damage threshold, the only option to achieve high total energy gains is to make the device longer. The largest current particle accelerators reach several of kilometers in length, requiring substantial resources to operate and maintain.

Dielectric laser acceleration (DLA) is an emerging method that seeks to revolutionize particle accelerator technology by exploiting decades of progress in nanofabrication, materials science, and laser technology. In DLA, periodic dielectric structures are illuminated with infrared laser light, which creates an electromagnetic field pattern in their vicinity that can accelerate electrically charged particles, such as electrons. When compared to metal surfaces at microwave frequencies, dielectric materials have very high damage thresholds at short pulse durations and infrared wavelengths [29, 43]. This allows DLAs to achieve energy gains per length that are 1 to 2 orders of magnitude higher than those found in conventional radio frequency (RF) accelerators. Experimental demonstrations of these acceleration gradients have been made practical in recent years by the availability of robust nanofabrication techniques combined with modern solid state laser systems [13].

As a result, the development of DLA can lead to compact particle accelerators that enable new applications. By providing the potential for generating relativistic electron beams in relatively short length scales, DLA technology is projected to have numerous applications where tabletop accelerators may be useful, including medical imaging, radiation therapy, and X-ray generation [37, 14]. To achieve high energy gain in a compact size, it is of principle interest to design structures that may produce the largest acceleration gradients possible without exceeding their respective damage thresholds.

Several recently demonstrated candidate DLA structures consist of a planar dielectric structure that is periodic along the particle axis with either an semi-open geometry or a narrow (micron to sub-micron) vacuum gap in which the particles travel [38, 35, 29, 26, 10, 7, 8, 24]. These structures are then side-illuminated by laser pulses. Fig. ?? shows a schematic of the setup, with a laser pulse incident from the bottom.

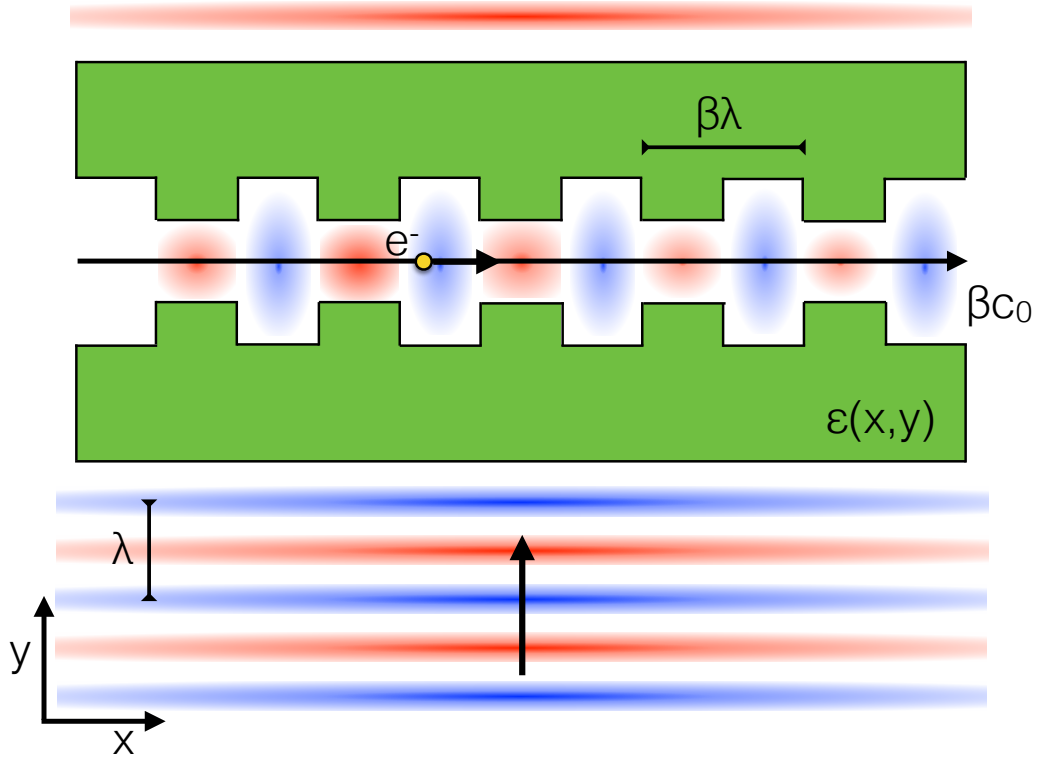


Figure 2.1: Diagram outlining the system setup for side-coupled DLA with an arbitrary dielectric structure  $\epsilon(x, y)$  (green). A charged particle moves through the vacuum gap with speed  $\beta c_0$ . The periodicity is set at  $\beta\lambda$  where  $\lambda$  is the central wavelength of the laser pulse.

The laser field may also be treated with a pulse front tilt [16, 3] to enable group velocity matching over a distance greater than the laser's pulse length. For acceleration to occur, the dielectric structure must be designed such that the particle feels an electric field that is largely parallel to its trajectory over many optical periods. In the following calculations, the geometry of the dielectric structure is represented by a spatially varying dielectric constant  $\epsilon(x, y)$ . We assume invariance in one coordinate ( $\hat{z}$ ) in keeping with the planar symmetry of most current designs. However the methodology we present can be extended to include a third dimension. In addition, our work approximates the incident laser pulse as a monochromatic plane wave at the central frequency, which is a valid approximation as long as the pulse duration is large compared to the optical period.

## 2.2 Adjoint Method for Particle Accelerators

Here we will discuss the use of the adjoint method to design such a structure, as explained in Ref. [1]. To begin, we must first define the optimization figure of merit and design parameters.

We first seek to maximize the *acceleration gradient* of the device, which is defined as the amount of energy gain per unit length achieved by a particle that is phased correctly with the driving field. In a general DLA device, the acceleration gradient ' $G$ ' over a time period ' $T$ ' is defined mathematically as

$$G = \frac{1}{T} \int_0^T E_{||}(\vec{r}(t), t) dt, \quad (2.1)$$

where  $\vec{r}(t)$  is the position of the electron and  $E_{||}$  signifies the (real) electric field component parallel to the electron trajectory at a given time.

Since we assume the structure is invariant in the  $\hat{z}$  direction, we may work in two dimensions, examining only the  $H_z$ ,  $E_x$  and  $E_y$  field components. While this approximation neglects fringing fields that will be present in any fabricated device, it is a good approximation for the fields experienced by particles traversing the center of the acceleration channel. For an approximately monochromatic input laser source with angular frequency  $\omega$ , the electric fields are, in general, of the form

$$\vec{E}(\vec{r}, t) = \Re \left\{ \tilde{E}(\vec{r}) e^{i\omega t} \right\}, \quad (2.2)$$

where  $\tilde{E}$  is complex-valued.

Let us assume the particle we wish to accelerate is moving on the line  $y = 0$  with velocity  $\vec{v} = \beta c_0 \hat{x}$ , where  $c_0$  is the speed of light in vacuum and  $\beta \leq 1$ . The  $x$  position of the particle as a function of time is given by  $x(t) = x_0 + \beta c_0 t$ , where  $x_0$  represents an arbitrary choice of initial starting position. For normal incidence of the laser (laser propagating in the  $+\hat{y}$  direction), phase velocity matching between the particle and the electromagnetic fields is established by introducing a spatial periodicity in our structure of period  $\beta\lambda$  along  $\hat{x}$ , where  $\lambda$  is the laser wavelength. In the

limit of an infinitely long structure (or equivalently,  $T \rightarrow \infty$ ) we may rewrite our expression for the gradient in Eq. (2.1) as an integral over one spatial period, given by

$$G = \frac{1}{\beta\lambda} \Re \left\{ e^{-i\phi_0} \int_0^{\beta\lambda} dx E_x(x, 0) e^{i\frac{2\pi}{\beta\lambda}x} \right\}. \quad (2.3)$$

Here the quantity  $\phi_0 = \frac{2\pi x_0}{\beta\lambda}$  is representative of the phase of the particle as it enters the spatial period. In further calculations, we set  $\phi_0 = 0$ , only examining the acceleration gradients experienced by particles entering the accelerator with this specific phase. Since we have arbitrarily control over our input laser phase, this does not impose any constraint on the acceleration gradient attainable.

To simplify the following derivations, we define the following inner product operation involving the integral over two vector quantities  $\vec{a}$  and  $\vec{b}$  over a single period volume  $V'$

$$\langle \vec{a}, \vec{b} \rangle = \int_{V'} dv. (\vec{a} \cdot \vec{b}) = \int_0^{\beta\lambda} dx \int_{-\infty}^{\infty} dy (\vec{a} \cdot \vec{b}). \quad (2.4)$$

With this definition, we then have the gradient

$$G = \Re \left\{ \langle \vec{E}, \vec{\eta} \rangle \right\}, \quad (2.5)$$

where we define the vector field ' $\vec{\eta}$ ' to signify the position and phase of the moving electron as

$$\vec{\eta}(x, y) = \frac{1}{\beta\lambda} e^{i\frac{2\pi}{\beta\lambda}x} \delta(y) \hat{x}. \quad (2.6)$$

The physical interpretation of  $\vec{\eta}$  is diagrammed in Fig. 2.2.

Our goal in designing the accelerator for maximum acceleration gradient is to create a permittivity distribution that maximizes  $G$  subject to a few constraints. We consider performing this optimization in a small design region surrounding a small gap defined for the electron to travel through the structure. Secondly, we assume that the structure has a finite extent along the direction of the incoming laser beam. We also consider realizing this device through the patterning of a material with permittivity  $\epsilon_{\max}$ . Therefore, the final device should have permittivity of either 1 or  $\epsilon_{\max}$  at all points.

To perform this optimization task, we may consider discretizing our entire spatial domain into a rectangular grid, which will be necessary for numerical simulation. As our design parameters,  $\phi$ , we take permittivity of each grid cell within the design region. Our problem then becomes finding the permittivity of each cell that will maximize the acceleration gradient, subject to each grid cell having a permittivity value of either 1 or  $\epsilon_{\max}$ .

To accomplish this, the simplest approach would involve doing a direct search over the full design space. For example, one could label each cell within the design region with an identifier '0' or '1' corresponding to 'vacuum' and 'material', respectively. Then, one may generate all possible

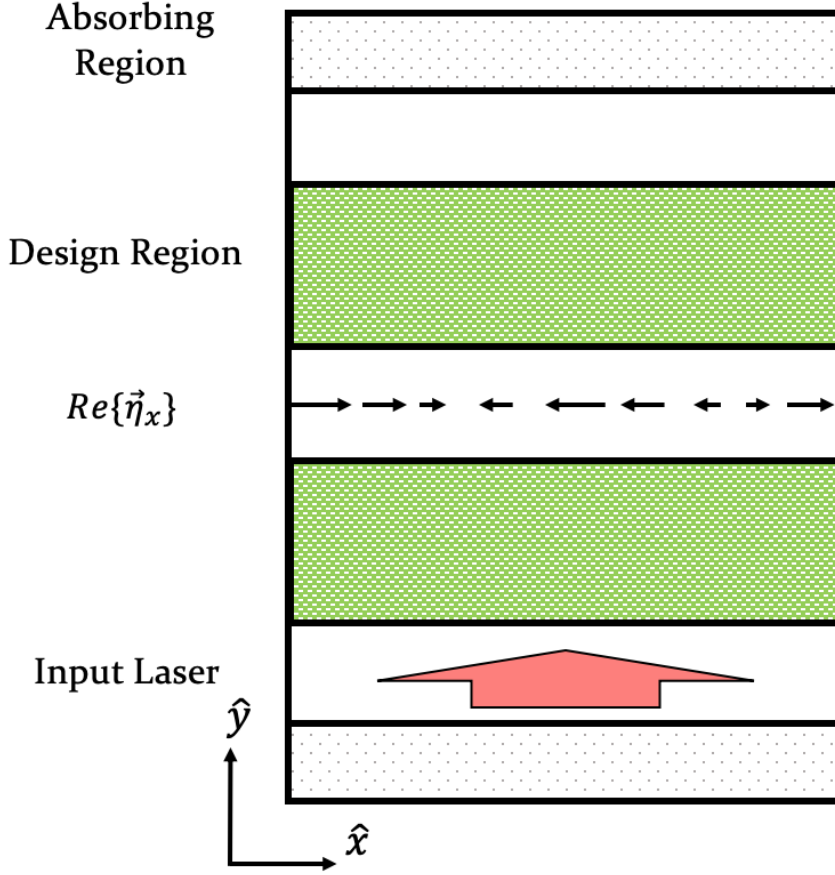


Figure 2.2: Definition of the vector field,  $\vec{\eta}$ , which defines the position of the electron in the frequency domain. The green regions represent domains where we will optimize the material properties using the adjoint method. The central gap is constrained to vacuum to allow passage of the electron beam. The red arrow signifies the driving laser.

structures and check their respective acceleration gradients. However, as one can imagine, this method would be far too computationally expensive to perform in practice. For example, even considering a very small design region consisting of  $10 \times 10 = 100$  grid cells would result in  $2^{100} \approx 10^{30}$  devices to simulate. While one may consider smart ways of searching through this device space without checking each structure, using global optimization approaches such as genetic algorithms [47] or particle swarm optimization [1], this problem is still quite computationally expensive and the size of design space becomes exponentially larger as the number of design parameters are increased.

A smarter approach involves *gradient-based optimization*, in which we search the design space according to the local gradient of the figure of merit with respect to each of the parameters. For example, we may start with an initially random device, compute how the performance will change

with respect to a change in the permittivity of each cell in the design region, and make a small update. This process may be repeated until convergence on a locally optimal solution. If the design space contains several local optima, then this whole process may be repeated several times with different initial conditions.

In fact, this method is the standard approach to training of neural networks, which may also be framed as an optimization problem over thousands to millions of parameters. We will revisit this connection in a later chapter. While the performance of gradient-based optimization is hard to directly compare to that of global optimization approaches, as the number of design parameters increases, gradient-based optimization are typically preferred as they require far fewer steps in most problems.

For gradient-based optimization to be useful, one would like an efficient means to compute the gradient of the figure of merit with respect to the design parameters. For neural networks, the gradient is computed analytically and then evaluated using the *backpropagation* algorithm [? ]. For photonic devices, one may perform a similar technique using the *adjoint method*, which allows one to analytically compute the gradient directly from Maxwell's Equations and evaluate the result with only one additional electromagnetic simulation. This remarkable efficiency is largely responsible for the success of inverse design in photonics.

The adjoint method is typically introduced for linear optical systems, although, as we will show in a later chapter, it may be extended to nonlinear systems without much additional complication. In the frequency domain, Maxwell's equations may be written as

$$\nabla \times \nabla \times \vec{E}(\vec{r}) - k_0^2 \epsilon_r(\vec{r}) \vec{E}(\vec{r}) \equiv A\vec{E}(\vec{r}) = -i\mu_0\omega\vec{J}(\vec{r}), \quad (2.7)$$

Here,  $\vec{E}(\vec{r})$  and  $\vec{J}(\vec{r})$  are the electric field and electric current distributions, respectively.  $k_0 = \omega/c_0$ ,  $\epsilon_r$  is the relative permittivity and a non-magnetic material is assumed ( $\mu = \mu_0$ ). This formalism is referred to as *finite-difference frequency-domain* (FDFD) [41, 44].

More abstractly, we may write Eq. (2.7) as

$$A\mathbf{x} = \mathbf{b}, \quad (2.8)$$

where  $A$  is a sparse, complex symmetric matrix that encodes Maxwell's equations on the device.

$\mathbf{x}$  is a vector containing the electromagnetic fields at each position in the domain, which are the solution to Eq. (2.8) given the vector  $\mathbf{b}$  describing the electric current source distribution in the domain.

Our device is described by a set of design variables  $\phi$ , which influence the system matrix,  $A = A(\phi)$ . Differentiating Eq. (2.7) with respect to  $\phi$ , and assuming that the current source,  $\mathbf{b}$ , does

not depend on  $\phi$ , we may recover the change in the solution with respect to the parameters as

$$\frac{d\mathbf{x}}{d\phi} = -A^{-1} \frac{\partial A}{\partial \phi} A^{-1} \mathbf{b} = -A^{-1} \frac{\partial A}{\partial \phi} \mathbf{x} \quad (2.9)$$

Now, we consider differentiating an objective function  $J = J(\mathbf{x})$  that depends explicitly on the field solution. By the chain rule, this gives

$$\frac{dJ}{d\phi} = -\Re \left\{ \frac{\partial J}{\partial \mathbf{x}} \frac{d\mathbf{x}}{d\phi} \right\} = -\Re \left\{ \frac{\partial J}{\partial \mathbf{x}} A^{-1} \frac{\partial A}{\partial \phi} \mathbf{x} \right\} \quad (2.10)$$

To evaluate Eq. (2.10), we define a second simulation with source term  $-\frac{\partial J^T}{\partial \mathbf{x}}$ ,

$$A^T \mathbf{x}_{\text{aj}} = A \mathbf{x}_{\text{aj}} = -\frac{\partial J^T}{\partial \mathbf{x}}, \quad (2.11)$$

then the field solution,  $\mathbf{x}_{\text{aj}} = -A^{-1} \frac{\partial J^T}{\partial \mathbf{x}}$ , can be easily identified in Eq. (2.10), which gives the expression

$$\frac{dG}{d\phi} = \Re \left\{ \mathbf{x}_{\text{aj}}^T \frac{\partial A}{\partial \phi} \mathbf{x} \right\}. \quad (2.12)$$

The only quantity in this expression that depends on the parameter  $\phi$  is  $\frac{\partial A}{\partial \phi}$ . As we will soon discuss, this quantity will generally be trivial to compute. On the other hand, the full field calculations of  $\mathbf{x}$  and  $\mathbf{x}_{\text{aj}}$  are computationally expensive, but may be computed once and used for an arbitrarily large set of parameters  $\phi_i$ . This gives the adjoint method significant scaling advantage with respect to traditional direct sensitivity methods, such as finite difference, which require a separate full-field calculation for each parameter being investigated.

Previously, we expressed the acceleration gradient as the inner product of the electric fields  $\vec{E}(\vec{r})$  and our vector field  $\vec{\eta}(\vec{r})$  as

$$G = \Re \left\{ \langle \vec{E}, \vec{\eta} \rangle \right\}, \quad (2.13)$$

which we may express in matrix notation as

$$G = \Re \left\{ \boldsymbol{\eta}^T \mathbf{x} \right\}, \quad (2.14)$$

where  $\boldsymbol{\eta}$  is a vector representing  $\vec{\eta}$  on the finite difference grid and  $\mathbf{x}$  is a vector containing the electric fields, as before.

In this notation, the adjoint problem is therefore

$$A^T \mathbf{x}_{\text{aj}} = -\frac{\partial G^T}{\partial \mathbf{x}} = -\boldsymbol{\eta}. \quad (2.15)$$

Intuitively, this represents a situation where the electric current source is located at the central

gap where the accelerator is traversing the structure. To make this point more explicit, let us now consider the fields radiated by a point particle of charge  $q$  flowing through our domain at  $y = 0$  with velocity  $\vec{v} = \beta c_0 \hat{x}$ . In the time domain, we can represent the current density of this particle as

$$\vec{J}_{\text{rad}}(x, y; t) = q\beta c_0 \delta(x - x_0 - c_0 \beta t) \delta(y) \hat{x}. \quad (2.16)$$

To express this in the frequency domain, we take the Fourier transform of  $\vec{J}_{\text{rad}}$  with respect to time, giving

$$\vec{J}_{\text{rad}}(x, y; \omega) = q\beta c_0 \delta(y) \hat{x} \int_{-\infty}^{\infty} dt \exp(-i\omega t) \delta(x - x_0 - c_0 \beta t) \quad (2.17)$$

$$= q \exp\left(i \frac{\omega (x - x_0)}{c_0 \beta}\right) \delta(y) \hat{x} \quad (2.18)$$

$$= q \exp\left(i \frac{2\pi}{\beta \lambda} x\right) \exp(-i\phi_0) \delta(y) \hat{x}. \quad (2.19)$$

Comparing with the source of our adjoint problem,  $\vec{J}_{\text{aj}} = \frac{-i}{\omega \mu_0} \vec{\eta}$ , we can see that

$$\vec{J}_{\text{aj}} = \frac{-i \exp(i\phi_0)}{2\pi q \beta c_0 \mu_0} \vec{J}_{\text{rad}}. \quad (2.20)$$

This finding shows that the adjoint field solution ( $\vec{E}_{\text{aj}}$ ) corresponds (up to a complex constant) to the field radiating from a test particle flowing through the accelerator structure. To put this another way, in order to calculate the acceleration gradient sensitivity with the adjoint problem, we must simulate the same structure operating both as an accelerator ( $A\vec{E} = -i\omega\mu_0\vec{J}_{\text{acc}}$ ) and as a radiator ( $A\vec{E}_{\text{aj}} = -i\omega\mu_0\vec{J}_{\text{aj}}$ ).

It is understood that one way to create acceleration is to run a radiative process in reverse. Indeed, this is the working principle behind accelerator schemes such as inverse free electron lasers [32, 11], inverse Cherenkov accelerators [22, 15], and inverse Smith-Purcell accelerators [5, 30]. Here, we see that this relationship can be expressed in an elegant fashion using the adjoint method.

We now confirm that the adjoint gradient matches the results obtained by direct sensitivity analysis, we examine a simple accelerator geometry composed of two opposing dielectric squares each of relative permittivity  $\epsilon$ . We take a single  $\phi$  parameter to be the relative permittivity of the entire square region. Because we only change the region inside the dielectric square, we may identify the  $\frac{\partial A}{\partial \phi}$  operator from Eq. (2.7) as

$$\frac{dA}{d\epsilon}(\vec{r}) = \begin{cases} -k_0^2 & \text{if } \vec{r} \text{ in square} \\ 0 & \text{otherwise} \end{cases}. \quad (2.21)$$

Thus, given the form of the sensitivity of the acceleration gradient from Eq. (2.12), combined



with Eq. (2.21), the change in acceleration gradient with respect to changing the entire square permittivity is simply given by the integral of the two field solutions over the square region, labeled ‘ $sq$ ’

$$\frac{dG}{d\epsilon_{sq}} = -k_0^2 \Re \left\{ \int_{sq} d^2\vec{r} \cdot \vec{E}(\vec{r}) \cdot \vec{E}_{aj}(\vec{r}) \right\}. \quad (2.22)$$

In Fig. Fig. 2.3 we compare this result with the direct sensitivity calculation where the system is manually changed and simulated again, using a finite difference derivative. The two methods agree with excellent precision, which confirms that the adjoint formalism is giving the correct results.

Extending this example to the general case of perturbing the permittivity at an arbitrary position  $\vec{r}$ , we see that

$$\frac{dG}{d\epsilon}(\vec{r}) = -k_0^2 \Re \left\{ \int d^2\vec{r}' \cdot \vec{E}(\vec{r}') \cdot \vec{E}_{aj}(\vec{r}') \cdot \delta(\vec{r} - \vec{r}') \right\} \quad (2.23)$$

$$= -k_0^2 \Re \left\{ \vec{E}(\vec{r}) \cdot \vec{E}_{aj}(\vec{r}) \right\}. \quad (2.24)$$

## 2.3 Inverse design of Dielectric Laser Accelerator

With the mathematical form of the adjoint problem discussed, now we focus on the optimization and inverse design of the DLA device. In our FDFD simulation, we use a grid spacing that corresponds to 200 grid points per free space wavelength in each dimension. Perfectly matched layers are implemented as absorbing regions on the edges parallel to the electron trajectory, with periodic boundary conditions employed on boundaries perpendicular to the electron trajectory. A total-field scattered-field [44] formalism is used to create a perfect plane wave input for the acceleration mode.

Since the adjoint method gives us a highly efficient method to calculate  $\frac{dG}{d\epsilon_i}$ , we use this information in an iterative optimization procedure. During each iteration, we first calculate  $\frac{dG}{d\epsilon_i}$  for all pixels ‘ $i$ ’ within some specified design region. Then, we update the  $\epsilon_i$  of each grid cell as follows

$$\epsilon_i := \epsilon_i + \alpha \frac{dG}{d\epsilon_i}. \quad (2.25)$$

Here,  $\alpha$  is a step parameter that we can tune. We need  $\alpha$  to be small enough to find local maxima, but large enough to have the optimization run in reasonable amount of time. This process is repeated until convergence on  $G$ , as diagrammed in Fig. 2.4.

During the course of optimization, the permittivity distribution is considered as a continuous variable, which is not realistic in physical devices. To address this issue, we employ a permittivity capping scheme during optimization. We define a maximum permittivity ‘ $\epsilon_m$ ’ corresponding to a material of interest. During the iterative process, if the relative permittivity of any cell becomes either less than 1 (vacuum) or greater than  $\epsilon_m$ , that cell is pushed back into the acceptable range.

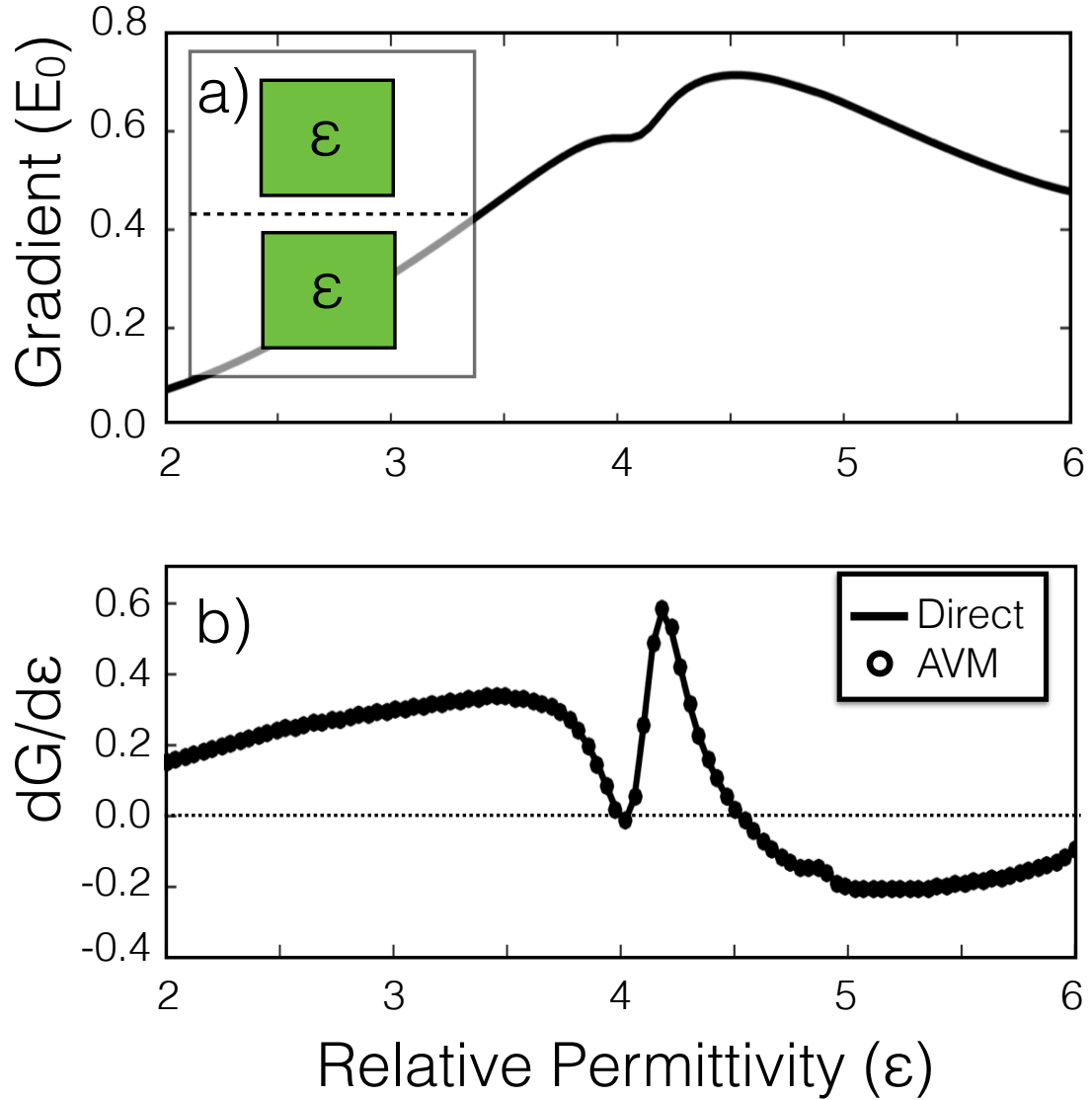


Figure 2.3: Demonstration of adjoint method in calculating accelerator sensitivities. (a) The acceleration gradient ( $G$ ) of a square accelerator structure (inset) as a function of the square's relative permittivity. We express the acceleration gradient in its dimensionless form, normalized by the electric field amplitude of the incident plane wave ( $E_0$ ). The particle traverses along the dotted line with a velocity of  $c_0$  ( $\beta = 1$ ) and a plane wave is incident from the bottom of the structure. (b) The sensitivity  $\frac{dG}{d\epsilon}$  of the gradient with respect to changing the square relative permittivity for direct central difference (solid line)  $\frac{dG}{d\epsilon} = \frac{G(\epsilon+\Delta\epsilon) - G(\epsilon-\Delta\epsilon)}{2\Delta\epsilon}$  and using the adjoint method (circles). The two calculations agree with excellent precision. The dotted line at  $\frac{dG}{d\epsilon} = 0$ , corresponds to local minima and maxima of  $G(\epsilon)$  above.

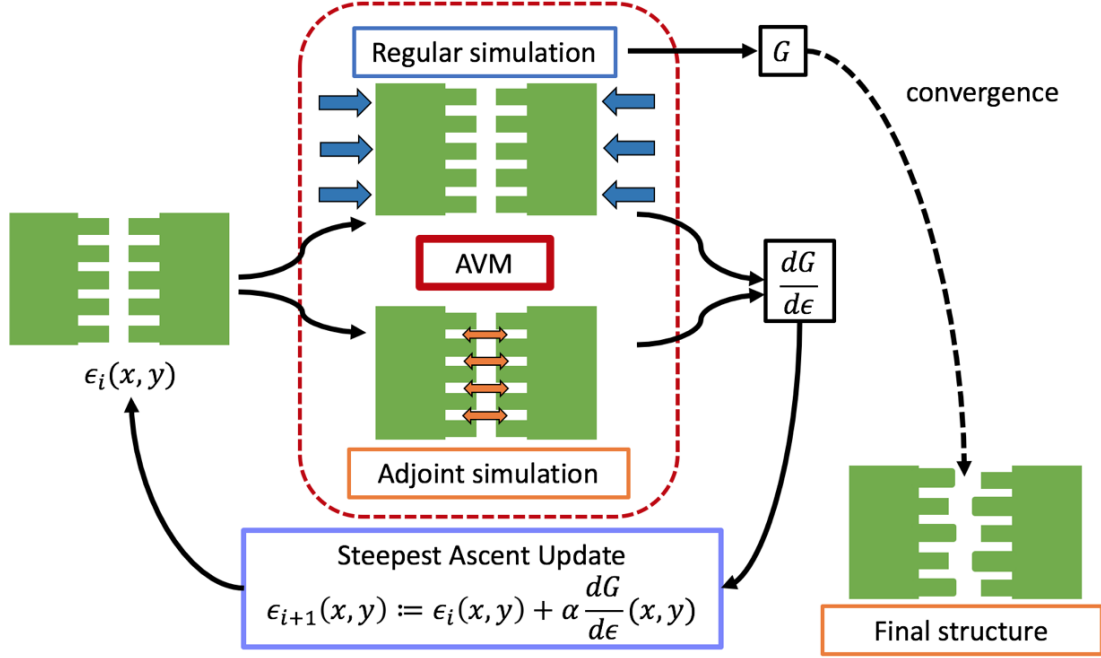


Figure 2.4: Optimization routine for DLA.

It was found that with this capping scheme, the structures converged to binary (each pixel being either vacuum or material with a permittivity of  $\epsilon_m$ ) after a number of iterations without specifying this choice of binary materials as a requirement of the optimization. Therefore, only minimal post-processing of the structures was required. Since high index contrast is favorable for maximizing the acceleration gradient, the optimization often favors increasing index contrast within the structure, which leads to each pixel being pushed towards either 1 or  $\epsilon_m$ . This is a possible explanation for why the structures converge to binary distributions under our optimization procedure.

The results of this optimization scheme are shown in Figs. 2.5(b)-2.5(d) for three different  $\epsilon_m$  values corresponding to commonly explored DLA materials. The design region was taken to be a rectangle fully surrounding but not including the particle gap. The design region was made smaller for higher index materials, since making it too large led to divergence during the iteration. We found that a totally vacuum initial structure worked well for these optimizations. However, initially random values between 1 and  $\epsilon_m$  for each pixel within the design region also gave reasonable results. For materials of Si, Si<sub>3</sub>N<sub>4</sub>, and SiO<sub>2</sub>, the achieved gradients (normalized by the incident field,  $E_0$ ) were 0.90, 0.56, and 0.31 ( $E_0$ ), respectively. Assuming incident field values consistent with the laser damage thresholds given in Ref. [43], these correspond to acceleration gradients of 0.25, 0.83, and 1.33 GV m<sup>-1</sup>, respectively. Without the dielectric mirrors, these structures give normalized acceleration gradients of 0.28, 0.15, and 0.07 ( $E_0$ ), respectively. For comparison, the Si dual pillar

structures presented in Ref. [26] give gradients of around 0.3 ( $E_0$ ). Therefore, the adjoint optimized structures show about a three-fold improvement in acceleration gradient over established structures.

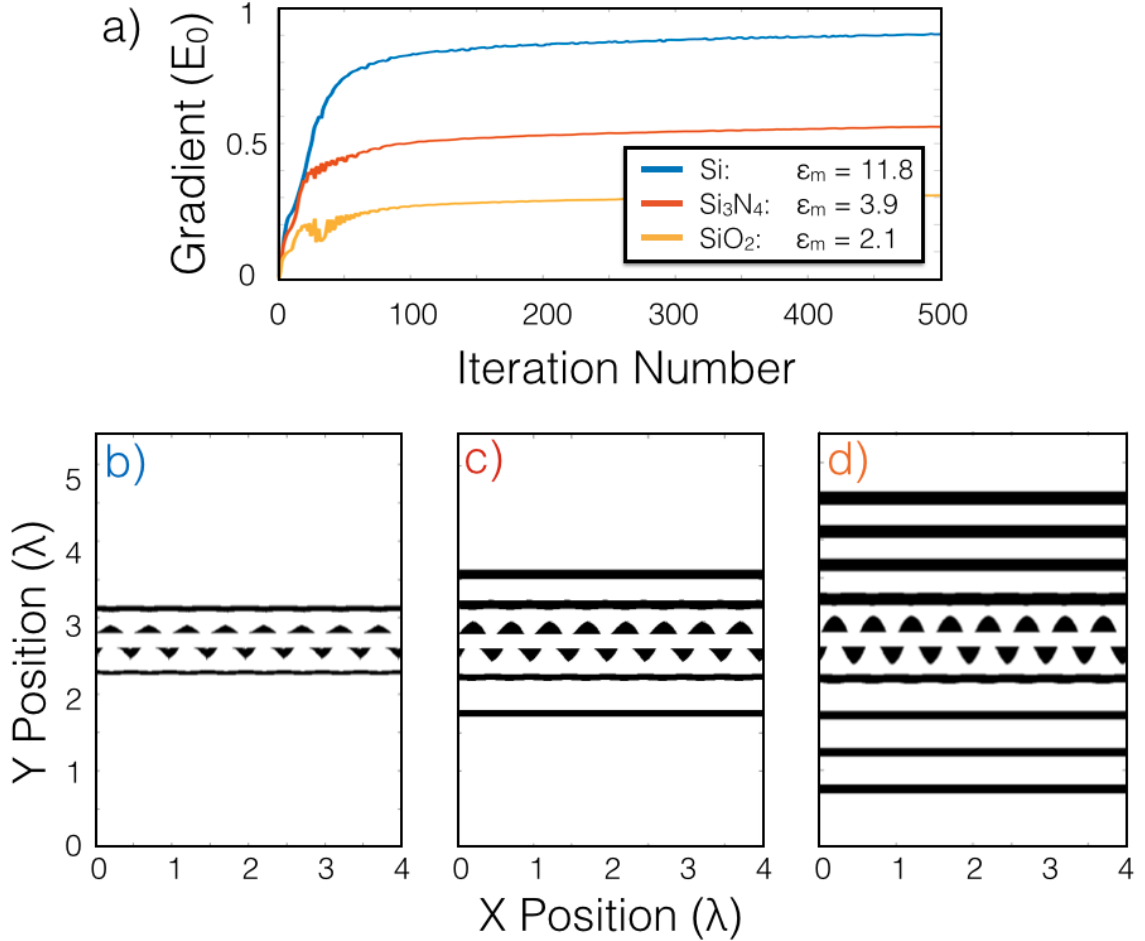


Figure 2.5: Demonstration of the structure optimization for  $\beta = 0.5$ , laser wavelength  $\lambda = 2 \mu\text{m}$ , and a gap size of 400 nm. A plane wave is incident from the bottom in all cases. (a) Acceleration gradient as a function of iteration number for different maximum relative permittivity values, corresponding to those of Si,  $\text{Si}_3\text{N}_4$ , and  $\text{SiO}_2$  at the laser wavelength. The acceleration gradient is normalized by the electric field amplitude of the incident plane wave ( $E_0$ ). The optimizations converge after about five-hundred iterations. (b-d) Final structure permittivity distributions (white = vacuum, black =  $\epsilon_m$ ) corresponding to the three curves in (a). Eight periods are shown, corresponding to four laser wavelengths. For each (b-d), design region widths on each side of the particle gap were given by 1, 2, and  $4 \mu\text{m}$  for Si,  $\text{Si}_3\text{N}_4$ , and  $\text{SiO}_2$ , respectively.

This optimization scheme seems to favor geometries consisting of a staggered array of field-reversing pillars surrounding the vacuum gap, which is already a popular geometry for DLA. However, these optimal designs also include reflective mirrors on either side of the pillar array, which

suggests that for strictly higher acceleration gradients, it is useful to use dielectric mirrors to resonantly enhance the fields in the gap.

It was observed that for random initial starting permittivity distributions, the same structures as shown in Fig. 2.5 are generated every time. Furthermore, as shown in Fig. 2.6, the geometries found using this method are remarkably similar to those recently proposed through human design using physical intuition [25]. These findings together suggest that the proposed structures may be close to the globally optimal structure for maximizing  $G$ .

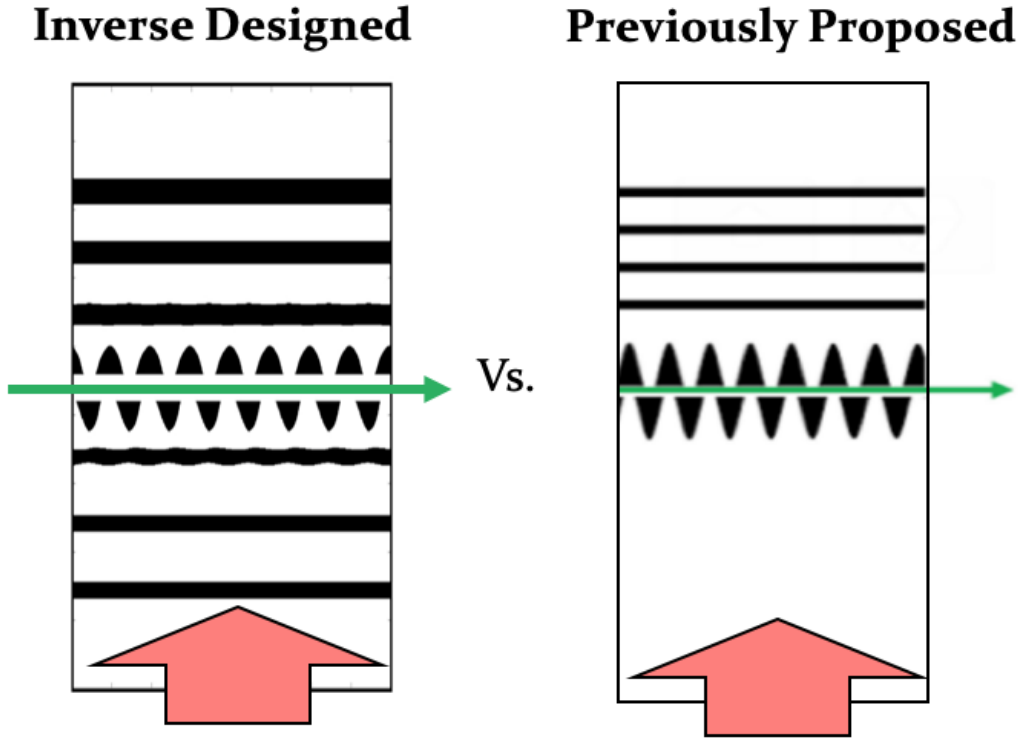


Figure 2.6: Similarity between DLA structures designed using adjoint method (left) and those independently proposed using human intuition.

It was further found that convergence could be achieved faster by a factor of about ten by including a ‘momentum’ term in the update equation. This term corresponds to the sensitivity calculated at the last iteration multiplied by a constant,  $\alpha' < 1$ . Explicitly, for iteration number ‘ $j$ ’ and pixel ‘ $i$ ’

$$\epsilon_i^{(j+1)} := \epsilon_i^{(j)} + \alpha \left[ \frac{dG^{(j)}}{d\epsilon_i} + \alpha' \frac{dG^{(j-1)}}{d\epsilon_i} \right]. \quad (2.26)$$

## 2.4 Optimization of acceleration factor

DLAs are often driven with the highest input field possible before damage occurs. Therefore, another highly relevant quantity to maximize is the *acceleration factor*, given by the acceleration gradient divided by the maximum electric field amplitude in the system. This quantity will ultimately limit the amount of acceleration gradient we can achieve when running at damage threshold. Explicitly, the acceleration factor is given by

$$f_A = \frac{G}{\max\{|\vec{E}|\}}. \quad (2.27)$$

Here,  $|\vec{E}|$  is a vector of electric field amplitudes in our system, which are normalized, as in the case of  $G$ , by the electric field amplitude of the incident plane wave ( $E_0$ ). The  $\max\{\}$  function is designed to pick out the highest value of this vector in either our design or material region, depending on the context. The *design region* is defined as the total region outside of the particle gap where the permittivity is updated. The *material region* is defined as any region where the permittivity is equal to  $\epsilon_m$ . We would like to use the same basic formalism to maximize  $f_A$ . However, since the  $\max\{\}$  function is not differentiable, this is not possible directly. Instead we may use a ‘smooth-max’ function to approximate  $\max\{\}$  as a weighted sum of vector components

$$\max\{|\vec{E}|\} \approx \frac{\sum_i |\vec{E}_i| \exp(a|\vec{E}_i|)}{\sum_i \exp(a|\vec{E}_i|)}. \quad (2.28)$$

Here, the parameter  $a \geq 0$  controls the relative strength of the exponential sum terms, for  $a = 0$ , this function simply gives the average value of the field amplitudes. By sweeping  $a$  and examining the acceleration factors of the resulting optimized structures, we determined that  $a = 3$  gave the best improvement in  $f_A$ . If  $a$  is too large, the calculation may induce floating point overflow or rounding error issues.

Using this smooth-max function, one may calculate  $\frac{df_A}{d\epsilon_i}$  analytically and perform structure optimizations in the same way that was discussed previously. The derivation of the adjoint source term is especially complicated and omitted for brevity, although the end result is expressed solely in terms of the original fields, the adjoint fields, and the  $\frac{dA}{d\gamma}$  operator, as before. Two structures with identical parameters but optimized, respectively, for maximum  $G$  and  $f_A$  are shown in Fig. 2.7. On the left, we see that the  $G$  maximized structure shows the characteristic dielectric mirrors, giving resonant field enhancement. On the right is the structure optimized for  $f_A$ , which has eliminated most of its dielectric mirrors and also introduces interesting pillar shapes. In Table 2.1 the main DLA performance quantities of interest are compared between these two structures. Whereas the acceleration gradient is greatly reduced when maximizing for  $f_A$ , the  $f_A$  value itself is improved by about 25% or 23% depending on whether one measures the maximum field in the design region or the material region, respectively. As a comparison with the geometry from Ref. [26], a SiO<sub>2</sub> dual

pillar structure with a 400 nm gap was optimized for acceleration gradient, giving an acceleration gradient of 0.025 ( $E_0$ ) with a pillar radius of 670 nm. This structure was found to have  $\max\{|\vec{E}|\}$  in the design region of 1.612 ( $E_0$ ) and  $\max\{|\vec{E}|\}$  in the material region of 1.209 ( $E_0$ ), leading to acceleration factors of 0.016 and 0.021, respectively. Comparing these numbers to those in Table 2.1, it is apparent that the AVM-optimized structures perform better than the dual pillar structures in terms of both gradient and acceleration factor.

These findings suggest that the inverse design strategy is effective in designing not only resonant, high acceleration gradient structures, but also non-resonant structures that are more damage resistant. In the future, when more components of DLA are moved on-chip (such as the optical power delivery), it will be important to have control over the resonance characteristics of the DLA structures to prevent damage breakdown at the input facet. Our technique may be invaluable in designing structures with tailor-made quality factors for this application.

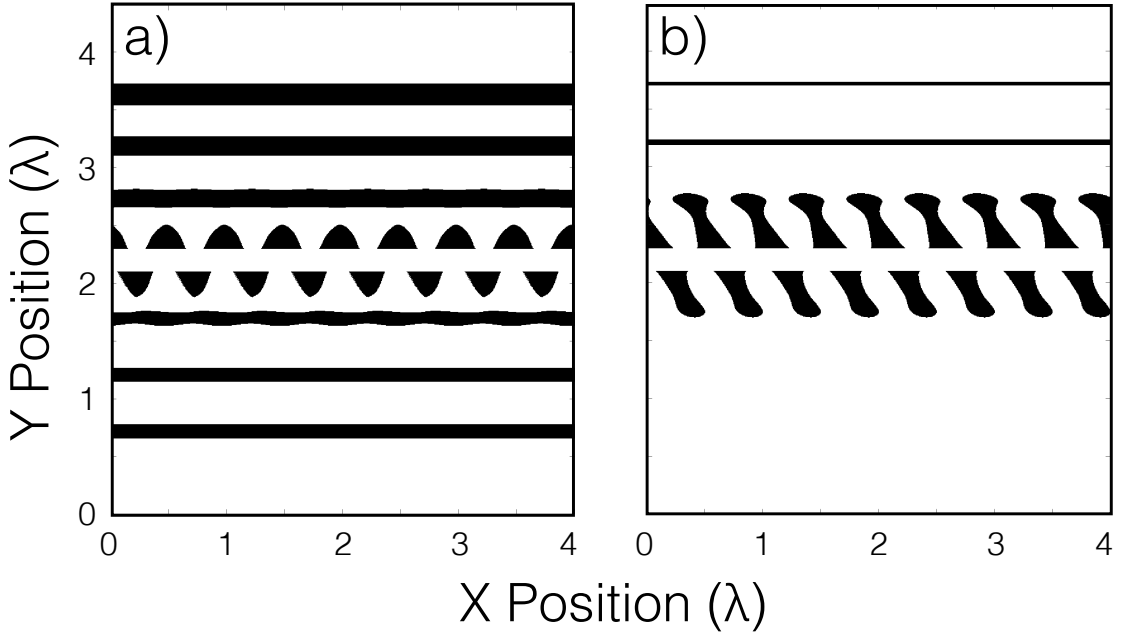


Figure 2.7: Demonstration of the final structures after optimization for (a) maximizing gradient only, (b) maximizing the acceleration factor.  $\beta = 0.5$ , laser wavelength  $\lambda = 2 \mu\text{m}$ , gap size of 400 nm.  $\epsilon_m = 2.1$ , corresponding to  $\text{SiO}_2$ . In (a), the high gradients are achieved using reflective dielectric mirrors to confine and enhance the fields in the center region. In (b), these dielectric mirrors are removed and the pillar structures are augmented. The structure in (b) shows a 23% increase in the acceleration factor in the material region when compared to (a).

Table 2.1: Acceleration factor ( $f_A$ ) before and after maximization.

Quantity	Value (max $G$ )	Value (max $f_A$ )	Chang.
Gradient ( $E_0$ )	0.1774	0.0970	-45.32%
$\max\{ \vec{E} \}$ in design region ( $E_0$ )	4.1263	1.7940	-56.52%
$\max\{ \vec{E} \}$ in material region ( $E_0$ )	2.7923	1.2385	-55.84%
$f_A$ in design region	0.0430	0.0541	+25.81%
$f_A$ in material region	0.0635	0.0783	+23.31%

## 2.5 Conclusions

We found that the adjoint method is a reliable method for optimizing DLA structures for both maximum acceleration gradient and also acceleration factor. The optimization algorithm discussed shows good convergence and rarely requires further post-processing of structures to create binary permittivity distributions. Therefore, it is a simple and effective method for designing DLAs. Whereas most structure optimization in this field uses parameter sweeps to search the design space, the efficiency of our method allows us to more intelligently find optimal geometries without shape parameterization. Furthermore, the structures that we design are fabricable.

Although no DLA structures have been tested at the proposed wavelength of  $2\mu\text{m}$ , both simulations [38] and experimental results from other wavelengths [26] show gradients far below those presented here. We had limited success designing DLA structures in the relativistic ( $\beta \approx 1$ ) regime, especially for higher index materials, such as Si. We believe this is largely due to the stronger coupling between electron beam and incident plane wave at this energy. The characteristics of the adjoint source change dramatically at the  $\beta = 1$  point. Whereas in the sub-relativistic regime, the adjoint source generates an evanescent near-field extending from the gap particle position, at  $\beta \geq 1$ , the adjoint fields become propagating by process of Cherenkov radiation. Upon using the above described algorithm, the gradients diverge before returning to low values, no matter the step size  $\alpha$ . The only way to mitigate this problem is to choose prohibitively small design regions or low index materials, such as  $\text{SiO}_2$ .

In addition to the side-incident geometry explored, this technique is applicable to designing other dielectric-based accelerator structures. This includes particle-laser co-propagating schemes [12] and dielectric wakefield acceleration [49], among others. Therefore, we expect that our results may find use in the larger advanced accelerator community.

In this chapter, we have introduced the adjoint variable method as a powerful tool for designing dielectric laser accelerators for high gradient acceleration and high acceleration factor. We have further shown that the adjoint simulation is sourced by a point charge flowing through the accelerator, which quantifies the reciprocal relationship between an accelerator and a radiator.

Optimization algorithms built on this approach allow us to search a substantially larger design space and generate structures that give acceleration gradients far above those normally used for



each material. Furthermore, the structures designed by adjoint are fundamentally not constrained by shape parameterization, allowing never-before-seen geometries to be generated and tested. This theme will continue to be explored in other chapters.

## Chapter 3

# Integrated Photonic Circuit for Accelerators on a Chip

In the previous chapter, we discussed the basic working principles of DLA and described its optimization using the adjoint method. Here, we will describe the use of integrated optics to power and control such a device over an extended length.

### 3.1 On-Chip Laser Coupling Device

As mentioned, since DLA structures are already driven at their damage thresholds, apart from finding methods to increase material damage thresholds, achieving high total energy gain from DLA will fundamentally require extending the interaction length between the incoming laser pulse and the particle beam. This interaction length is limited not only by the longitudinal and transverse stability of the electron beam [? ?], but also by the laser delivery system, which is the focus of this work. Several proof of principle DLA experiments [? 35] have demonstrated high acceleration gradients using free-space manipulation of the laser pulse, including lensing, pulse-front-tilting [16, 3?], or multiple driving lasers [? 29]. However, these techniques require extensive experimental effort to perform and the system is exceedingly sensitive to angular alignment, thermal fluctuations, and mechanical noise. By replacing free-space manipulation with precise nano-fabrication techniques, an on-chip laser power delivery system would allow for orders of magnitude increases in the achievable interaction lengths and energy gains from DLA.

In designing any laser power delivery system for DLA, there are a few major requirements to consider. (1) The optical power spatial profile must have good overlap with the electron beam side profile. (2) The laser pulses must be appropriately delayed along the length of the accelerator to arrive at the same time as the moving electron bunches. (3) The optical fields along each section

of the accelerator must, ideally, be of the correct phase to avoid dephasing between the electrons and incoming laser fields. To accomplish all three of these requirements, we introduce a method for on-chip power delivery, which is based on a fractal *tree-network* geometry. Furthermore, we provide a systematic study of the structure's operating principles, the optimal range of operating parameters, and the fundamental trade-offs that must be considered for any on-chip laser coupling strategy of the same class [? ]. Through detailed numerical modeling of this design, we estimate that the proposed structure may achieve 1 MeV of energy gain over a distance less than 1 cm by sequentially illuminating 49 identical structures.

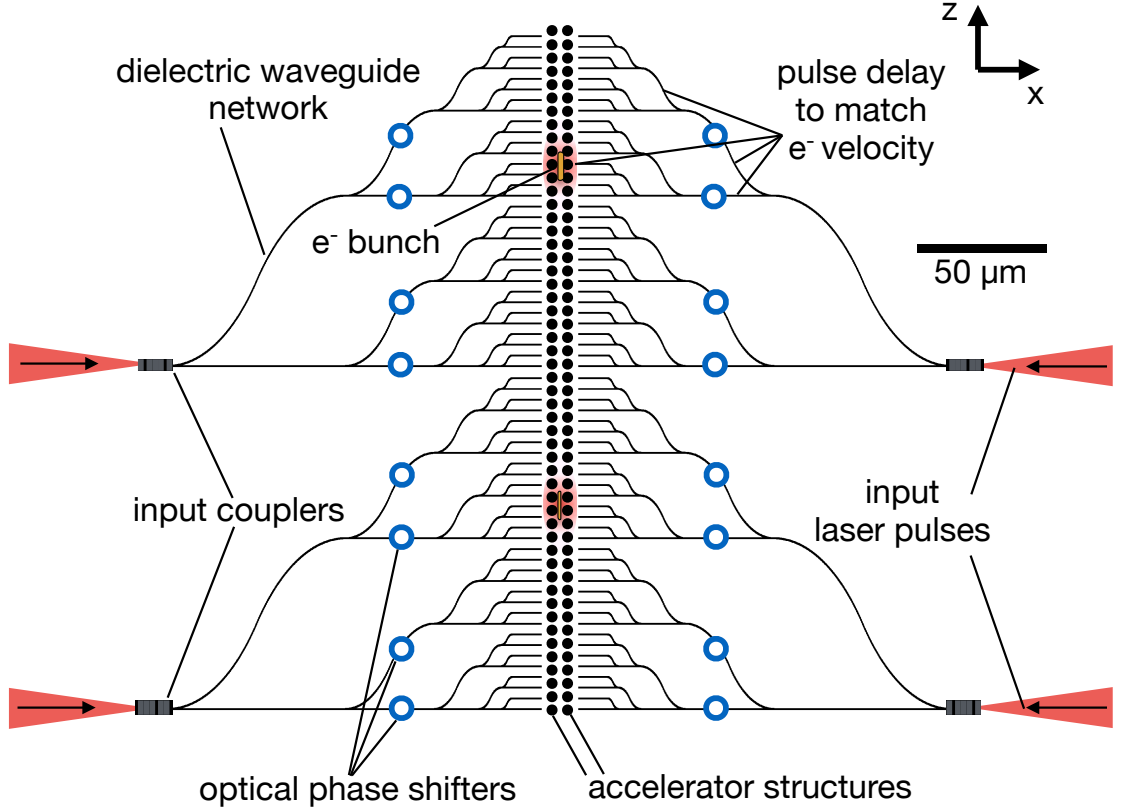


Figure 3.1: Two stages of the DLA laser coupling ‘tree-network’ structure. The electron beam travels along the z-axis through the center of this structure. The laser pulses are side coupled with optical power shown in red. Black regions define the on-chip waveguide network. Blue circles represent the optical phase shifters used to tune the phase of the laser pulse. This geometry serves to reproduce the pulse-front-tilt laser delivery system outlined in [? ] in an integrated optics platform.

We first introduce the proposed *tree-network* waveguide geometry, which is diagrammed in Fig. 3.1. The electron beam to be accelerated is propagating along the z-axis in the central accelerator gap. We first couple the laser pulses to the on-chip dielectric waveguides by use of input couplers. The optical power is then split a series of times and directed by waveguide bends to illuminate

the entire length of the accelerator gap. Integrated phase shifters are used to tune the phase of each pulse upon exiting the waveguides and may be optimized for maximum acceleration. The accelerating structures are placed adjacent to the waveguide outputs. In this study, we choose to investigate silicon dual-pillar accelerator structures, similar to those used in [26]. The entire device is mirrored over the center plane and is driven by laser inputs on each side. Two stages of the structure are shown in Fig. 3.1, although several more may be implemented in series, assuming availability of several phase-locked laser sources. Electron beam focusing elements may be implemented between stages as needed.

We will now discuss the individual components involved in the on-chip laser coupling system.

### 3.1.1 Input Coupling

The proposed structure first requires a strategy to couple light from the pump laser to the on-chip optical waveguides. We focus on free-space coupling to the input facet via a surface grating, eliminating the need for single mode fiber delivery. Our laser and macroscopic optical components are capable of handling pulse energies far beyond enough to cause damage to the structure. Bare single mode fibers also have damage thresholds high enough to withstand these laser pulses, but the large amount of dispersion introduced (associated with the relatively long length of  $> 1$  mm) will make them unsuitable for delivery to the chip.

In general, couplers must have (1) high coupling efficiency, (2) a bandwidth large enough to couple entire pulse spectrum, and (3) high power handling and minimized hot spots. Input coupling may be accomplished by use of end coupling, focusing the laser beam directly onto the waveguide cross section, or vertical coupling schemes, such as grating couplers. In SOI systems, end coupling can achieve insertion losses as low as 0.66 dB (85.9%) over a bandwidth of roughly 10 THz [? ], but is cumbersome to perform experimentally for a large number of inputs and constrains the input and output coupling ports to be located on the edges of the chip. Vertical couplers provide the benefit of relative flexibility in alignment and positioning on chip. The coupling efficiency of these devices varies drastically depending on the complexity of the grating coupler design, from an efficiency of  $> 30\%$  to  $> 90\%$  [? ]. However, highly efficient broadband couplers capable of sustaining large bandwidths still provide design challenges, with the state-of-the-art fully-etched structures able to provide 67% coupling efficiency with a 3 dB bandwidth of 60 nm at 1550 nm [? ].

In this study, we assume a coupling power efficiency of 60% with a substantially wide bandwidth to accommodate that of our pulse (up to about 117 nm for a 50 fs pulse), which is reasonably achievable with end coupling. Additional investigation into the design of ultra-broadband vertical couplers must be considered to guarantee coupling of the femtosecond pulsed lasers.

### 3.1.2 Waveguides

Waveguides are a critical component of laser coupling. Schematics of the waveguide cross-sections and their field distributions are shown in Fig. 3.2. We have explored two general classes of waveguiding systems: (1) tightly confined systems and (2) weakly confined systems. Weakly confined waveguide modes have a small difference between mode effective index and cladding index, which results in the optical power being spread over a larger area and into the cladding material, which generally has preferable damage and nonlinearity properties. However, as we will discuss in the next section, our simulations show that weakly confined modes, with  $n_{\text{eff}} - n_{\text{core}}$  of about 0.1, have almost 0% power transmission for bend radii less than 10  $\mu\text{m}$ . In our tree-network structure, we require bend radii on this order to achieve the required pulse delay to matching to the electron bunch, therefore weakly guided waveguides were not considered for the particular tree-network structure in this parameter study.

We explored material systems of SOI and  $\text{Si}_3\text{N}_4/\text{SiO}_2$  due to their common use as waveguide core materials. SOI-based waveguides would be simpler to integrate with the silicon DLA structure and electron gun and there exists a much larger body of previous work on fabrication of silicon material systems for applications such as phase control, especially in the LIDAR community [? ?]. However,  $\text{Si}_3\text{N}_4/\text{SiO}_2$  waveguides have favorable nonlinear and damage properties when compared to SOI. As mentioned, there are several other material systems that could also be explored for low loss, low nonlinearity, and high damage thresholds.  $\text{Ta}_2\text{O}_5$  [?] and  $\text{Ga}_2\text{O}_3$  are promising candidates that will be investigated in future studies.

### 3.1.3 Splitters

After the initial input coupling step, splitters are used to distribute the laser power along the DLA structure. Splitters further contribute to insertion loss. Experimental characterization of Y-splitters indicate losses on the order of 1 dB [?]. However, recent advances in topology optimization techniques have allowed for new designs with much higher efficiencies. Using *particle swarm optimization* [?], devices have been produced with theoretical insertion losses of 0.13 dB and an experimentally determined value of  $0.28 \pm 0.02$  dB [?]. As even more sophisticated techniques of optimization have been developed, the insertion loss of simulated designs has reached 0.07 dB [?]. Adjoint-based optimization methods have been further expanded to enforce fabrication constraints on the permitted designs, thus allowing one to expect greater agreement between simulated and fabricated structures [?]. As a consequence of the rapid progress made in this field and the efforts to ensure robustness of device to fabrication tolerance, we have used an insertion loss per splitter of 0.22 dB, or 95% efficiency, for the parameter study.

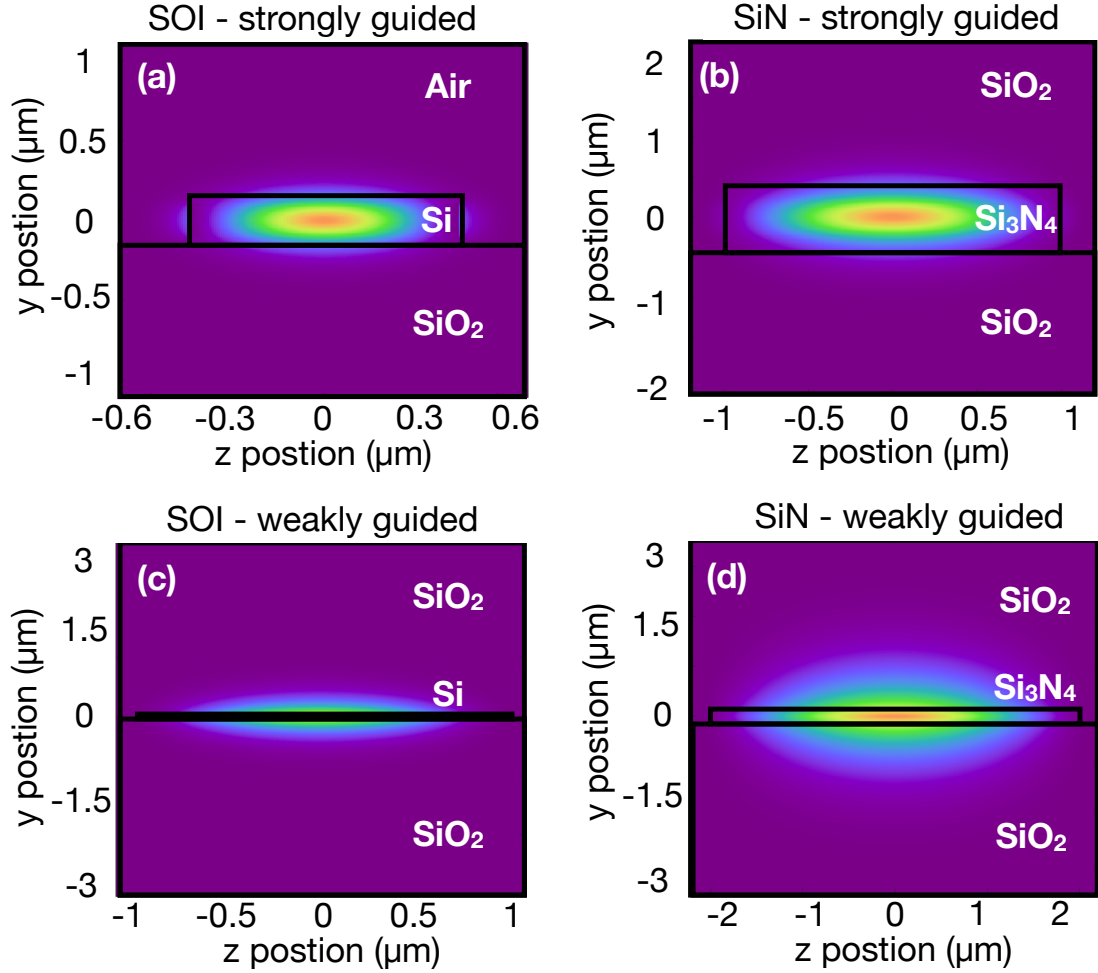


Figure 3.2: Waveguide geometries and corresponding horizontal electric field components [? ]. (a-b) Strongly confined modes. (c-d) Weakly confined modes. (a) and (c) are SOI material platforms whereas (b) and (d) are  $\text{Si}_3\text{N}_4/\text{SiO}_2$  materials. Waveguide core heights in (a-d) are given by 220, 400, 60, and 100 nm, respectively. Waveguide core widths are given by 0.78, 1.6, 2, and 4  $\mu\text{m}$ , respectively.

### 3.1.4 Bends

The bending radius is uniquely chosen to give enough extra propagation distance to provide a delay of the pulse between different output ports, which is matched to the electron velocity. We derive conditions on the radius of curvature required for each bend for the particular tree-network structure in Appendix ?? . The required radius depends on the electron velocity ( $\beta c_0$ ) and group index of the waveguide mode ( $n_g$ ), and becomes smaller as the waveguides approach the DLA structure. Assuming the tree-network geometry used in this work, there is a condition on the group index of

the waveguide system that may achieve the required delay given an electron speed

$$n_g \beta \geq 1. \quad (3.1)$$

Thus, for sub-relativistic electrons ( $\beta < 1$ ), higher index materials are required for the waveguides. For example, for a  $\beta$  of  $1/3$ , a group index of  $n_g > 3$  is required, which may not be satisfied by a standard SiN waveguide geometry. Thus, in sub-relativistic regimes, SOI waveguides are the optimal choice.

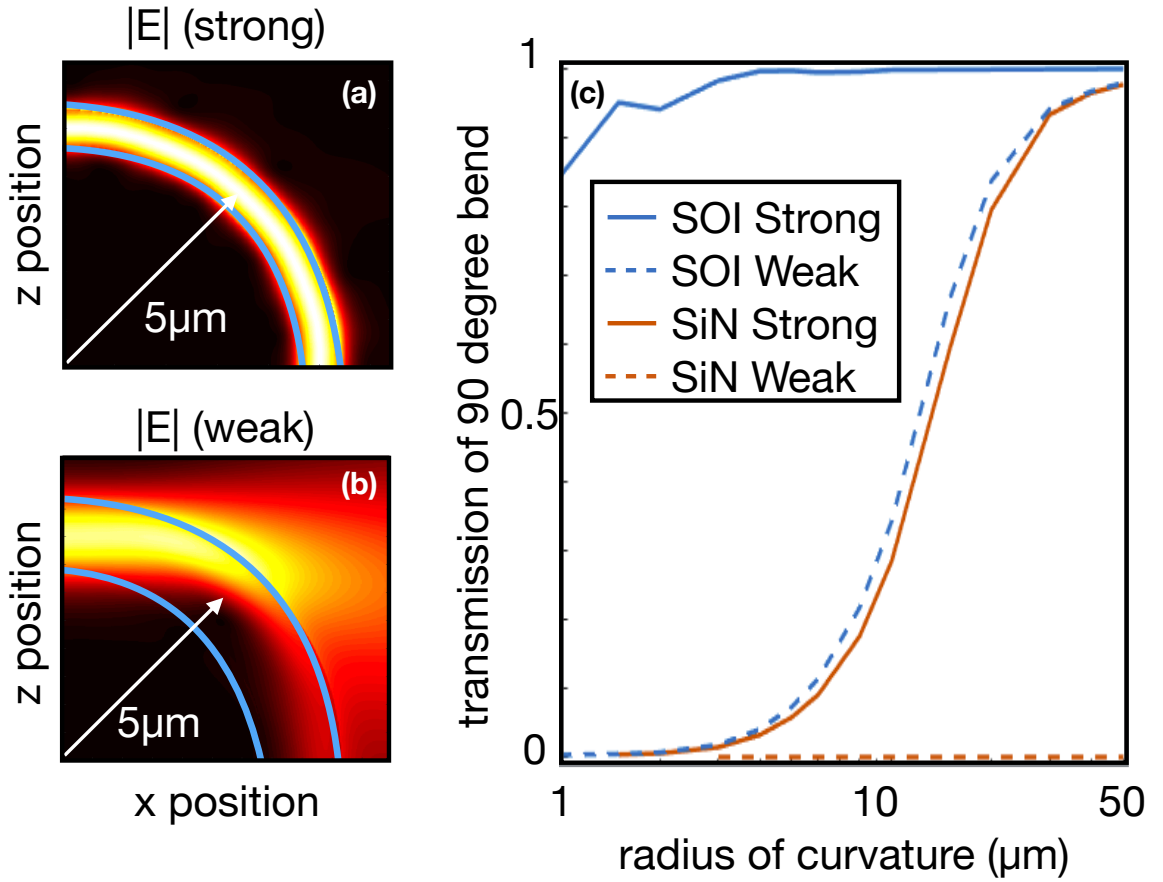


Figure 3.3: (a) Electric field amplitude for a strongly guiding SOI waveguide. (b) Electric field amplitude for a weakly guiding SOI waveguide. (c) Comparison of bending loss as a function of bend radius for the 4 waveguides from Fig. 3.2.

Fig. 3.3 shows the optical power transmission through a series of bends and waveguide geometries using the finite-difference frequency-domain method (FDFD) [41] and an established two-dimensional approximation to the three-dimensional structure [? ]. For tightly confined SOI waveguide modes, the bending radius can reach as low as 2  $\mu\text{m}$  before there is significant loss. However, for weakly

confined SOI modes and strongly confined SiN modes, the power transmission is less than 50% until the radius exceeds  $20\text{ }\mu\text{m}$ . For our purposes, this kind of bending loss is unacceptable as radii on the order of  $10\text{ }\mu\text{m}$  are required close to the DLA structure to perfectly match the electron velocity. However, if we relax the delay requirement in favor of larger bend radii, we may still use strongly confined SiN modes. Based on a calculation following Appendix ??, if we wish to keep all SiN waveguides above  $40\text{ }\mu\text{m}$  radius of curvature, we will experience a 25 fs mismatch in peak pulse arrival to electron arrival. For a pulse duration of 250 fs, this will have negligible effect on the acceleration gradient. Therefore, in our parameter study, we assume strongly confined waveguide modes and bends that are large enough to achieve transmission of 95%. Many of these issues may be reconciled by choosing a hybrid waveguide system, as shown in Fig. ??, in which different materials and waveguide modes are used at different distances from the central DLA structure. We did not consider these options directly in our following parameter study.

### 3.1.5 Phase Shifters

Phase shifters are an essential component in the DLA system for ensuring proper phase matching between the electrons and photons. While it is simple to do phase tuning in free-space for a single stage DLA with macroscopic delay stages, waveguide-integrated phase shifters for long interaction or multi-stage DLAs will be experimentally complicated. To achieve a sizable energy gain and gradient over a given interaction length, a high level of precision and stability in the phase of each section is required.

To illuminate the importance of precision phase shifters, a Monte Carlo simulation was performed in which the output phase of each waveguide was perturbed from its optimal value by a random amount. This study found that, for a stage length of 1 mm, phase stability and precision of greater than  $1/100$  of a radian (0.16% of a cycle) was required to achieve sustained energy gain within 90% of the maximum achievable amount.

There are a few strategies to implement integrated phase shifters, including the use of (1) thermal/thermal-optic effect [??], (2) electro-optic effect, and (3) mechanical techniques, such as piezo controlled elements [?]. For this application, we will require a full  $2\pi$  range of phase control of each output port with a resolution of  $1/100$  of a radian, and a modulation bandwidth of  $\sim 1\text{ kHz}$  to correct for environmental perturbations.

Rather than supplying each waveguide output port with a phase shifter with these properties, it may be possible to have dedicated ‘fine’ and ‘coarse’ phase shifters as we move through the splitting structure. Furthermore, some degree of relative fixed phase between output ports may be accomplished by precision fabrication.

To further mitigate the challenges associated with operating these multiple phase shifters during acceleration, we may implement a feedback control loop, which is described in Fig. 3.4. In this setup, the quantity of interest, such as electron energy gain, can be measured at the end of a section





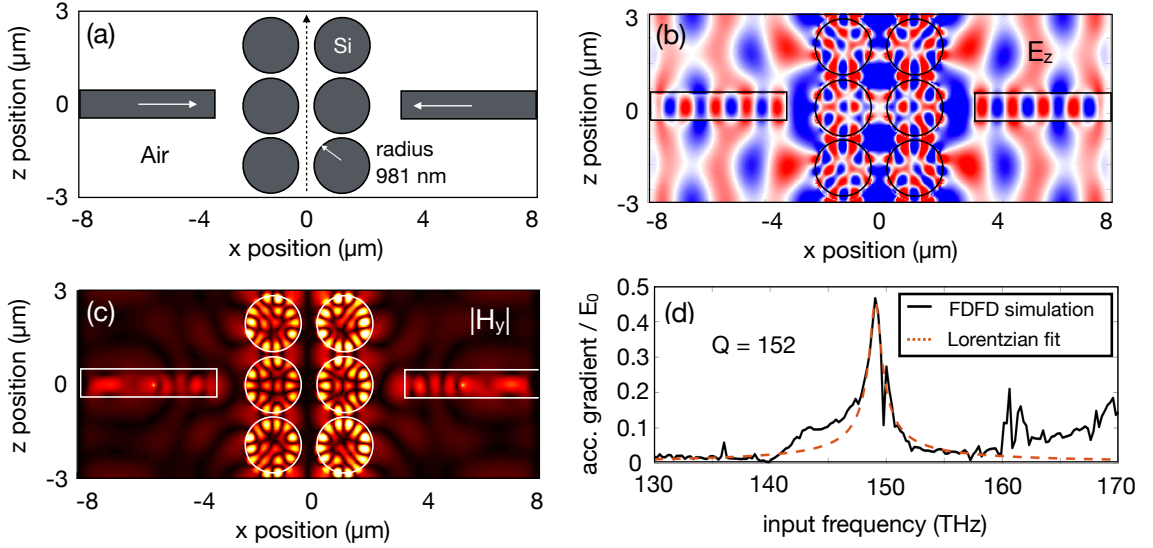


Figure 3.5: (a) A schematic of the waveguide to DLA connection. Silicon dual pillars of optimized radius of 981 nm and gap size of 400 nm are used. (b) The accelerating electric field during one time step. (c) Absolute value of the transverse magnetic field. (d) Absolute value of the acceleration gradient as a function of frequency, normalized by the peak electric field in the waveguide. A Lorentzian line shape is fit to the square of this plot. The square root of this fit is shown in red. Based on the Lorentzian fit, a Q-factor of  $152 \pm 29$  was determined. As computed following the derivation in [38], but with the waveguide mode impedance and effective area in place of the plane wave values, this structure has a shunt impedance,  $Z_S$ , of 449.1  $\Omega$  over 3 periods and a  $Z_S/Q$  value of 2.95  $\Omega$ .

the spacing and radius parameters. It is also clear that the two surrounding DLA cells are slightly out of phase with the center cell. This effect is caused by the lack of translational symmetry in the input optical beam in the  $z$  direction and will lower the acceleration gradient. From our Lorentzian fit, a Q value of  $152 \pm 29$  was determined.

Coupling efficiently from waveguides to DLA structures may be done by optimizing the structure parameters. For an optimized structure, back reflection may be minimized. It will be of great importance in future experiments to integrate the waveguide system and the DLA structure on the same chip. Thus, the height of the pillar structure may be constrained to be equal to that of the waveguide core and 500 nm thick SOI platforms may be a good starting point for testing these integrated systems.

One waveguide is able to serve multiple DLA periods. However, simulations suggest that additional periods of DLA per waveguide do not significantly increase the total energy gain achievable from a single waveguide. Thus, the spacing between waveguides must be large enough to eliminate cross-talk, but small enough to ensure high acceleration gradients.

### 3.1.7 Beam Loading and Longitudinal Wakes

The fundamental unit cell of the proposed accelerator design, depicted in Fig. ??, consists of a structure segment of three periods  $\Delta z = 3\lambda$  fed by a single laser pulse of the multi-branch network with duration  $\tau = 250$  fs. It is shown in Ref. [38] that the coupling efficiency of the laser field to a point charge  $q$  for the side-coupled geometry used here is analogous to Eq. (7) of Ref. [?], which considers a traveling wave mode in a cylindrical structure with group velocity  $\beta_g c$ , under the substitution  $\beta_g/(1 - \beta_g) \rightarrow \Delta z/\tau c$ , which gives a coupling efficiency  $\eta_q = qG\Delta z/P\tau$ . Here  $P$  is the laser mode power and  $G = G_0 - G_H$  is the loaded gradient where  $G_0$  is the unloaded value and  $G_H$  is a retarding field that accounts for the longitudinal wake induced in the structure by the beam. These may be written

$$G_0 = \sqrt{\frac{Z_C P}{\lambda^2}} \quad , \quad G_H = \frac{qcZ_H}{\lambda^2}. \quad (3.2)$$

where  $Z_C$  is the characteristic impedance and  $Z_H$  is the Cherenkov wake impedance. A conservative approximation for the latter  $Z_H \approx \pi Z_0 \lambda^2/(16a^2)$  is provided by Ref. [?] for the case of a flat (2D) geometry with a beam charge  $q$  in a narrow channel, where  $Z_0$  is the impedance of free space and we take  $a = 200$  nm to be the half-width of the accelerating channel. The resulting efficiency  $\eta_q$  is then quadratic in the charge  $q$ . Solving for the maximal value gives optimal bunch charge and efficiency

$$q_{\text{opt}} = \frac{G_0 \lambda^2}{2cZ_H} \quad , \quad \eta_{q_{\text{opt}}} = \frac{1}{4} \frac{\Delta z}{c\tau} \frac{Z_C}{Z_H}. \quad (3.3)$$

For the present case, with  $Z_C = 149\Omega$ ,  $Z_H = 7402\Omega$ ,  $G_0 = 108$  MV/m, we obtain  $q_{\text{opt}} \approx 0.1$  fC and  $\eta_{q_{\text{opt}}} \approx 0.04\%$ , corresponding to a retarding gradient  $G_H = 54$  MV/m and thus a beam loaded gradient  $G = G_0/2$ . The optimal charge corresponds to 608 electrons, which is consistent with achieved laser-triggered emission from nanotip electron sources. As shown in [?] under multi-bunch operation with structures designed for higher gradients, efficiencies can theoretically be in the tens of percents. The structure design considered here was intended to illustrate the basic principles of constructing a multi-guided wave system and was not optimized for efficient beam coupling. Even so, efficiencies this order are still acceptable for possible near-term applications, such as a 1 to 10 MeV medical linac, where requisite beam powers are less than 1 Watt.

### 3.1.8 Heat Dissipation

The laser input pulse energy at each stage of length  $L = 192 \mu\text{m}$  is  $E_p = 11$  nJ for the SiN case of Table ?. We assume a repetition rate  $f_{\text{rep}} = 10$  MHz, which is consistent with commercially available solid state fiber lasers at micro-Joule pulse energies. Given that there are two input laser couplings per stage of length  $L$  in the configuration of Fig. 3.1, the average laser power per unit length of accelerator is  $dP/dz \approx 11$  W/cm. Making a conservative assumption that all of this power passes through solid silicon, which has an absorption coefficient of  $\alpha_{\text{Si}} = 0.027 \text{ cm}^{-1}$  at  $\lambda = 2 \mu\text{m}$ , the

corresponding absorbed power is of order  $6 \text{ mW/cm}^2$ . This is more than 5 orders of magnitude lower than the technological limit for heat dissipation from planar surfaces where  $1 \text{ kW/cm}^2$  is typical [? ? ]. Prior work has shown that near-critical coupling to silicon dielectric accelerator structures using SOI waveguides is possible with appropriate phase adjustment to produce a traveling wave match between input and output couplers [? ]. The latter work was for a structure design based on a 3D photonic crystal, but illustrates the principle that more sophisticated power handling techniques can potentially be employed in future designs to remove laser power from the wafer and safely dump it away from the accelerator.

## 3.2 Parameter Study

## 3.3 Automatic Controlled Power Delivery Systems

### 3.3.1 Phase Control Mechanism

### 3.3.2 Power Control Mechanism using Reconfigurable Circuit

Deterministic Tuning Algorithm

Scaling Gains

## 3.4 Experimental Efforts

### 3.4.1 Waveguide Damage and Nonlinearity Measurements

### 3.4.2 Demonstration of Waveguide-Coupled Acceleration



## Chapter 4

# Training of Optical Neural Networks

### 4.1 Introduction to Machine Learning

#### 4.1.1 Applications

#### 4.1.2 Hardware Demands

### 4.2 Linear Nanophotonic Processors

### 4.3 Optical Neural Networks

#### 4.3.1 Conventional Neural Network

#### 4.3.2 Optical Integration

#### 4.3.3 Training Protocols

Computer Model Training

Brute Force Training

### 4.4 In Situ Backpropagation Training

#### 4.4.1 Derivation Using Adjoint Method

#### 4.4.2 Method for Measurement of Adjoint Gradient

#### 4.4.3 Numerical Demonstrations

### 4.5 Electro-Optic Activation Functions

#### 4.5.1 Motivation

#### 4.5.2 Research Activation Functions

## Chapter 5

# Extension of Adjoint Method beyond Linear Time-Invariant Systems.

### 5.1 Nonlinear Devices

#### 5.1.1 Generalization of Adjoint Method to Nonlinear Problems

#### 5.1.2 Inverse Design of Nonlinear Photonic Switches

### 5.2 Active Devices

#### 5.2.1 Adjoint Sensitivity for Multi-Frequency FDTD Problems

#### 5.2.2 Inverse Design of Optical Isolators through Dynamic Modulation

### 5.3 Adjoint for Time Domain

#### 5.3.1 Derivation

#### 5.3.2 Challenges

### 5.4 Forward-mode Differentiation

## Chapter 6

# Conclusion and Final Remarks



## Appendix A

# Something

Some appendix section.

# Bibliography

- [1] Particle swarm optimization: developments, applications and resources - IEEE Conference Publication.
- [2] Govind P. Agrawal. *Fiber-Optic Communication Systems*. John Wiley & Sons, February 2012.
- [3] Selcuk Akturk et al. Pulse-front tilt caused by spatial and temporal chirp. *Opt. Express*, 12(19):4399–4410, 2004.
- [4] Mordecai Avriel. *Nonlinear programming: analysis and methods*. Courier Corporation, 2003.
- [5] J Bae et al. Experimental verification of the theory on the inverse Smith–Purcell effect at a submillimeter wavelength. *Appl. Phys. Lett.*, 61(7):870–872, 1992.
- [6] P. I. Borel, A. Harpøth, L. H. Frandsen, M. Kristensen, P. Shi, J. S. Jensen, and O. Sigmund. Topology optimization and fabrication of photonic crystal structures. *Optics Express*, 12(9):1996–2001, May 2004.
- [7] John Breuer et al. Dielectric laser acceleration of electrons in the vicinity of single and double grating structures-theory and simulations. *J. Phys. B: At. Mol. Opt. Phys.*, 47(23):234004, 2014.
- [8] John Breuer et al. Dielectric laser acceleration of nonrelativistic electrons at a single fused silica grating structure: Experimental part. *Phys. Rev. ST Accel. Beams*, 17(2):021301, 2014.
- [9] D. E. Carlson and C. R. Wronski. Amorphous silicon solar cell. *Applied Physics Letters*, 28(11):671–673, June 1976.
- [10] Chia-Ming Chang and Olav Solgaard. Silicon buried gratings for dielectric laser electron accelerators. *Appl. Phys. Lett.*, 104(18):184102, 2014.
- [11] E. D. Courant et al. High-energy inverse free-electron laser accelerator. *AIP Conf. Proc.*, 127(1):849–874, 1985.

- [12] Benjamin M Cowan. Three-dimensional dielectric photonic crystal structures for laser-driven acceleration. *Phys. Rev. ST Accel. and Beams*, 11(1):011301, 2008.
- [13] Jay W Dawson et al. Analysis of the scalability of diffraction-limited fiber lasers and amplifiers to high average power. *Opt. Express*, 16(17):13240–13266, 2008.
- [14] R Joel England et al. Dielectric laser accelerators. *Rev. Mod. Phys.*, 86(4):1337, 2014.
- [15] J R Fontana and R H Pantell. A high-energy, laser accelerator for electrons using the inverse Cherenkov effect. *J. Appl. Phys.*, 54(8):4285–4288, 1983.
- [16] J Hebling. Derivation of the pulse front tilt caused by angular dispersion. *Opt. Quant. Electron.*, 28(12):1759–1763, 1996.
- [17] Po-Chun Hsu, Alex Y. Song, Peter B. Catrysse, Chong Liu, Yucan Peng, Jin Xie, Shanhui Fan, and Yi Cui. Radiative human body cooling by nanoporous polyethylene textile. *Science*, 353(6303):1019–1023, September 2016.
- [18] B. Jalali and S. Fathpour. Silicon Photonics. *Journal of Lightwave Technology*, 24(12):4600–4615, December 2006.
- [19] Antony Jameson. Aerodynamic Shape Optimization Using the Adjoint Method. page 30.
- [20] J. S. Jensen, O. Sigmund, L. H. Frandsen, P. I. Borel, A. Harpoth, and M. Kristensen. Topology design and fabrication of an efficient double 90/spl deg/ photonic Crystal waveguide bend. *IEEE Photonics Technology Letters*, 17(6):1202–1204, June 2005.
- [21] Jan Kern, Ruchira Chatterjee, Iris D. Young, Franklin D. Fuller, Louise Lassalle, Mohamed Ibrahim, Sheraz Gul, Thomas Fransson, Aaron S. Brewster, Roberto Alonso-Mori, Rana Hussein, Miao Zhang, Lacey Douthit, Casper de Lichtenberg, Mun Hon Cheah, Dmitry Shevela, Julia Wersig, Ina Seuffert, Dimosthenis Sokaras, Ernest Pastor, Clemens Weninger, Thomas Kroll, Raymond G. Sierra, Pierre Aller, Agata Butryn, Allen M. Orville, Mengning Liang, Alexander Batyuk, Jason E. Koglin, Sergio Carbajo, Sébastien Boutet, Nigel W. Moriarty, James M. Holton, Holger Dobbek, Paul D. Adams, Uwe Bergmann, Nicholas K. Sauter, Athina Zouni, Johannes Messinger, Junko Yano, and Vittal K. Yachandra. Structures of the intermediates of Kok’s photosynthetic water oxidation clock. *Nature*, 563(7731):421, November 2018.
- [22] W D Kimura et al. Laser acceleration of relativistic electrons using the inverse Cherenkov effect. *Phys. Rev. Lett.*, 74(4):546, 1995.
- [23] Diederik P. Kingma and Jimmy Ba. Adam: A Method for Stochastic Optimization. *arXiv:1412.6980 [cs]*, December 2014. arXiv: 1412.6980.

- [24] M Kozák et al. Dielectric laser acceleration of sub-relativistic electrons by few-cycle laser pulses. *Nucl. Instrum. Methods Phys. Res., Sect. A*, 2016. DOI: 10.1016/j.nima.2016.12.051.
- [25] Martin Kozak. Status report erlangen (hommelhoff group). ACHIP 3rd Collaboration Meeting, 2016.
- [26] Kenneth J Leedle et al. Dielectric laser acceleration of sub-100 keV electrons with silicon dual-pillar grating structures. *Opt. Lett.*, 40(18):4344–4347, 2015.
- [27] LIGO Scientific Collaboration and Virgo Collaboration, B. P. Abbott, R. Abbott, T. D. Abbott, M. R. Abernathy, F. Acernese, K. Ackley, C. Adams, T. Adams, P. Addesso, R. X. Adhikari, V. B. Adya, C. Affeldt, M. Agathos, K. Agatsuma, N. Aggarwal, O. D. Aguiar, L. Aiello, A. Ain, P. Ajith, B. Allen, A. Allocca, P. A. Altin, S. B. Anderson, W. G. Anderson, K. Arai, M. A. Arain, M. C. Araya, C. C. Arceneaux, J. S. Areeda, N. Arnaud, K. G. Arun, S. Ascenzi, G. Ashton, M. Ast, S. M. Aston, P. Astone, P. Aufmuth, C. Aulbert, S. Babak, P. Bacon, M. K. M. Bader, P. T. Baker, F. Baldaccini, G. Ballardín, S. W. Ballmer, J. C. Barayoga, S. E. Barclay, B. C. Barish, D. Barker, F. Barone, B. Barr, L. Barsotti, M. Barsuglia, D. Barta, J. Bartlett, M. A. Barton, I. Bartos, R. Bassiri, A. Basti, J. C. Batch, C. Baune, V. Bavigadda, M. Bazzan, B. Behnke, M. Bejger, C. Belczynski, A. S. Bell, C. J. Bell, B. K. Berger, J. Bergman, G. Bergmann, C. P. L. Berry, D. Bersanetti, A. Bertolini, J. Betzwieser, S. Bhagwat, R. Bhandare, I. A. Bilenko, G. Billingsley, J. Birch, R. Birney, O. Birnholtz, S. Biscans, A. Bisht, M. Bitossi, C. Biwer, M. A. Bizouard, J. K. Blackburn, C. D. Blair, D. G. Blair, R. M. Blair, S. Bloemen, O. Bock, T. P. Bodiya, M. Boer, G. Bogaert, C. Bogan, A. Bohe, P. Bojtos, C. Bond, F. Bondu, R. Bonnand, B. A. Boom, R. Bork, V. Boschi, S. Bose, Y. Bouffanais, A. Bozzi, C. Bradaschia, P. R. Brady, V. B. Braginsky, M. Branchesi, J. E. Brau, T. Briant, A. Brillet, M. Brinkmann, V. Brisson, P. Brockill, A. F. Brooks, D. A. Brown, D. D. Brown, N. M. Brown, C. C. Buchanan, A. Buikema, T. Bulik, H. J. Bulten, A. Buonanno, D. Buskulic, C. Buy, R. L. Byer, M. Cabero, L. Cadonati, G. Cagnoli, C. Cahillane, J. Calderón Bustillo, T. Callister, E. Calloni, J. B. Camp, K. C. Cannon, J. Cao, C. D. Capano, E. Capocasa, F. Carbognani, S. Caride, J. Casanueva Diaz, C. Casentini, S. Caudill, M. Cavaglià, F. Cavalier, R. Cavalieri, G. Cella, C. B. Cepeda, L. Cerboni Baiardi, G. Cerretani, E. Cesarini, R. Chakraborty, T. Chalermongsak, S. J. Chamberlin, M. Chan, S. Chao, P. Charlton, E. Chassande-Mottin, H. Y. Chen, Y. Chen, C. Cheng, A. Chincarini, A. Chiummo, H. S. Cho, M. Cho, J. H. Chow, N. Christensen, Q. Chu, S. Chua, S. Chung, G. Ciani, F. Clara, J. A. Clark, F. Cleva, E. Coccia, P.-F. Cohadon, A. Colla, C. G. Collette, L. Cominsky, M. Constancio, A. Conte, L. Conti, D. Cook, T. R. Corbitt, N. Cornish, A. Corsi, S. Cortese, C. A. Costa, M. W. Coughlin, S. B. Coughlin, J.-P. Coulon, S. T. Countryman, P. Couvares, E. E. Cowan, D. M. Coward, M. J. Cowart, D. C. Coyne, R. Coyne, K. Craig, J. D. E. Creighton, T. D. Creighton, J. Cripe, S. G.

Crowder, A. M. Cruise, A. Cumming, L. Cunningham, E. Cuoco, T. Dal Canton, S. L. Danilishin, S. D'Antonio, K. Danzmann, N. S. Darman, C. F. Da Silva Costa, V. Dattilo, I. Dave, H. P. Daveloza, M. Davier, G. S. Davies, E. J. Daw, R. Day, S. De, D. DeBra, G. Debreczeni, J. Degallaix, M. De Laurentis, S. Deléglise, W. Del Pozzo, T. Denker, T. Dent, H. Dereli, V. Dergachev, R. T. DeRosa, R. De Rosa, R. DeSalvo, S. Dhurandhar, M. C. Díaz, L. Di Fiore, M. Di Giovanni, A. Di Lieto, S. Di Pace, I. Di Palma, A. Di Virgilio, G. Dojcinoski, V. Dolique, F. Donovan, K. L. Dooley, S. Doravari, R. Douglas, T. P. Downes, M. Drago, R. W. P. Dr-ever, J. C. Driggers, Z. Du, M. Ducrot, S. E. Dwyer, T. B. Edo, M. C. Edwards, A. Effler, H.-B. Eggenstein, P. Ehrens, J. Eichholz, S. S. Eikenberry, W. Engels, R. C. Essick, T. Etzel, M. Evans, T. M. Evans, R. Everett, M. Factourovich, V. Fafone, H. Fair, S. Fairhurst, X. Fan, Q. Fang, S. Farinon, B. Farr, W. M. Farr, M. Favata, M. Fays, H. Fehrmann, M. M. Fejer, D. Feldbaum, I. Ferrante, E. C. Ferreira, F. Ferrini, F. Fidecaro, L. S. Finn, I. Fiori, D. Fiorucci, R. P. Fisher, R. Flaminio, M. Fletcher, H. Fong, J.-D. Fournier, S. Franco, S. Frasca, F. Frasconi, M. Frede, Z. Frei, A. Freise, R. Frey, V. Frey, T. T. Fricke, P. Fritschel, V. V. Frolov, P. Fulda, M. Fyffe, H. A. G. Gabbard, J. R. Gair, L. Gammaitoni, S. G. Gaonkar, F. Garufi, A. Gatto, G. Gaur, N. Gehrels, G. Gemme, B. Gendre, E. Genin, A. Gennai, J. George, L. Gergely, V. Germain, Abhirup Ghosh, Archisman Ghosh, S. Ghosh, J. A. Giaime, K. D. Giardina, A. Giazotto, K. Gill, A. Glaefke, J. R. Gleason, E. Goetz, R. Goetz, L. Gondan, G. González, J. M. Gonzalez Cas-tro, A. Gopakumar, N. A. Gordon, M. L. Gorodetsky, S. E. Gossan, M. Gosselin, R. Gouaty, C. Graef, P. B. Graff, M. Granata, A. Grant, S. Gras, C. Gray, G. Greco, A. C. Green, R. J. S. Greenhalgh, P. Groot, H. Grote, S. Grunewald, G. M. Guidi, X. Guo, A. Gupta, M. K. Gupta, K. E. Gushwa, E. K. Gustafson, R. Gustafson, J. J. Hacker, B. R. Hall, E. D. Hall, G. Ham-mond, M. Haney, M. M. Hanke, J. Hanks, C. Hanna, M. D. Hannam, J. Hanson, T. Hardwick, J. Harms, G. M. Harry, I. W. Harry, M. J. Hart, M. T. Hartman, C.-J. Haster, K. Haughian, J. Healy, J. Heefner, A. Heidmann, M. C. Heintze, G. Heinzl, H. Heitmann, P. Hello, G. Hem-ming, M. Hendry, I. S. Heng, J. Hennig, A. W. Heptonstall, M. Heurs, S. Hild, D. Hoak, K. A. Hodge, D. Hofman, S. E. Hollitt, K. Holt, D. E. Holz, P. Hopkins, D. J. Hosken, J. Hough, E. A. Houston, E. J. Howell, Y. M. Hu, S. Huang, E. A. Huerta, D. Huet, B. Hughey, S. Husa, S. H. Huttner, T. Huynh-Dinh, A. Idrisy, N. Indik, D. R. Ingram, R. Inta, H. N. Isa, J.-M. Isac, M. Isi, G. Islas, T. Isogai, B. R. Iyer, K. Izumi, M. B. Jacobson, T. Jacqmin, H. Jang, K. Jani, P. Jaranowski, S. Jawahar, F. Jiménez-Forteza, W. W. Johnson, N. K. Johnson-McDaniel, D. I. Jones, R. Jones, R. J. G. Jonker, L. Ju, K. Haris, C. V. Kalaghatgi, V. Kalogera, S. Kand-hasamy, G. Kang, J. B. Kanner, S. Karki, M. Kasprzack, E. Katsavounidis, W. Katzman, S. Kaufer, T. Kaur, K. Kawabe, F. Kawazoe, F. Kéfélian, M. S. Kehl, D. Keitel, D. B. Kel-ley, W. Kells, R. Kennedy, D. G. Keppel, J. S. Key, A. Khalaidovski, F. Y. Khalili, I. Khan, S. Khan, Z. Khan, E. A. Khazanov, N. Kijbunchoo, C. Kim, J. Kim, K. Kim, Nam-Gyu Kim,

Namjun Kim, Y.-M. Kim, E. J. King, P. J. King, D. L. Kinzel, J. S. Kissel, L. Kleybolte, S. Klimenko, S. M. Koehlenbeck, K. Kokeyama, S. Koley, V. Kondrashov, A. Kontos, S. Koranda, M. Korobko, W. Z. Korth, I. Kowalska, D. B. Kozak, V. Kringel, B. Krishnan, A. Królak, C. Krueger, G. Kuehn, P. Kumar, R. Kumar, L. Kuo, A. Kutynia, P. Kwee, B. D. Lackey, M. Landry, J. Lange, B. Lantz, P. D. Lasky, A. Lazzarini, C. Lazzaro, P. Leaci, S. Leavey, E. O. Lebigot, C. H. Lee, H. K. Lee, H. M. Lee, K. Lee, A. Lenon, M. Leonardi, J. R. Leong, N. Leroy, N. Letendre, Y. Levin, B. M. Levine, T. G. F. Li, A. Libson, T. B. Littenberg, N. A. Lockerbie, J. Logue, A. L. Lombardi, L. T. London, J. E. Lord, M. Lorenzini, V. Lorette, M. Lormand, G. Losurdo, J. D. Lough, C. O. Lousto, G. Lovelace, H. Lück, A. P. Lundgren, J. Luo, R. Lynch, Y. Ma, T. MacDonald, B. Machenschalk, M. MacInnis, D. M. Macleod, F. Magaña-Sandoval, R. M. Magee, M. Mageswaran, E. Majorana, I. Maksimovic, V. Malvezzi, N. Man, I. Mandel, V. Mandic, V. Mangano, G. L. Mansell, M. Manske, M. Mantovani, F. Marchesoni, F. Marion, S. Márka, Z. Márka, A. S. Markosyan, E. Maros, F. Martelli, L. Martellini, I. W. Martin, R. M. Martin, D. V. Martynov, J. N. Marx, K. Mason, A. Masserot, T. J. Massinger, M. Masso-Reid, F. Matichard, L. Matone, N. Mavalvala, N. Mazumder, G. Mazzolo, R. McCarthy, D. E. McClelland, S. McCormick, S. C. McGuire, G. McIntyre, J. McIver, D. J. McManus, S. T. McWilliams, D. Meacher, G. D. Meadors, J. Meidam, A. Melatos, G. Mendell, D. Mendoza-Gandara, R. A. Mercer, E. Merilh, M. Merzougui, S. Meshkov, C. Messenger, C. Messick, P. M. Meyers, F. Mezzani, H. Miao, C. Michel, H. Middleton, E. E. Mikhailov, L. Milano, J. Miller, M. Millhouse, Y. Minenkov, J. Ming, S. Mirshekari, C. Mishra, S. Mitra, V. P. Mitrofanov, G. Mitselmakher, R. Mittleman, A. Moggi, M. Mohan, S. R. P. Mohapatra, M. Montani, B. C. Moore, C. J. Moore, D. Moraru, G. Moreno, S. R. Morris, K. Mossavi, B. Mours, C. M. Mow-Lowry, C. L. Mueller, G. Mueller, A. W. Muir, Arunava Mukherjee, D. Mukherjee, S. Mukherjee, N. Mukund, A. Mullavey, J. Munch, D. J. Murphy, P. G. Murray, A. Mytidis, I. Nardecchia, L. Naticchioni, R. K. Nayak, V. Nacula, K. Nedkova, G. Nelemans, M. Neri, A. Neunzert, G. Newton, T. T. Nguyen, A. B. Nielsen, S. Nissanke, A. Nitz, F. Nocera, D. Nolting, M. E. N. Normandin, L. K. Nuttall, J. Oberling, E. Ochsner, J. O'Dell, E. Oelker, G. H. Oggin, J. J. Oh, S. H. Oh, F. Ohme, M. Oliver, P. Oppermann, Richard J. Oram, B. O'Reilly, R. O'Shaughnessy, C. D. Ott, D. J. Ottaway, R. S. Ottens, H. Overmire, B. J. Owen, A. Pai, S. A. Pai, J. R. Palamos, O. Palashov, C. Palomba, A. Pal-Singh, H. Pan, Y. Pan, C. Pankow, F. Pannarale, B. C. Pant, F. Paoletti, A. Paoli, M. A. Papa, H. R. Paris, W. Parker, D. Pascucci, A. Pasqualetti, R. Passaquieti, D. Passuello, B. Patricelli, Z. Patrick, B. L. Pearlstone, M. Pedraza, R. Pedurand, L. Pekowsky, A. Pele, S. Penn, A. Perreca, H. P. Pfeiffer, M. Phelps, O. Piccinni, M. Pichot, M. Pickenpack, F. Piergiovanni, V. Pierro, G. Pillant, L. Pinard, I. M. Pinto, M. Pitkin, J. H. Poeld, R. Poggiani, P. Popolizio, A. Post, J. Powell, J. Prasad, V. Predoi, S. S. Premachandra, T. Prestegard, L. R. Price, M. Prijatelj, M. Principe, S. Privitera, R. Prix, G. A. Prodi, L. Prokhorov, O. Puncken, M. Punturo, P. Puppato, M. Pürrer, H. Qi, J. Qin, V. Quetschke,

E. A. Quintero, R. Quitzow-James, F. J. Raab, D. S. Rabeling, H. Radkins, P. Raffai, S. Raja, M. Rakhmanov, C. R. Ramet, P. Rapagnani, V. Raymond, M. Razzano, V. Re, J. Read, C. M. Reed, T. Regimbau, L. Rei, S. Reid, D. H. Reitze, H. Rew, S. D. Reyes, F. Ricci, K. Riles, N. A. Robertson, R. Robie, F. Robinet, A. Rocchi, L. Rolland, J. G. Rollins, V. J. Roma, J. D. Romano, R. Romano, G. Romanov, J. H. Romie, D. Rosińska, S. Rowan, A. Rüdiger, P. Ruggi, K. Ryan, S. Sachdev, T. Sadecki, L. Sadeghian, L. Salconi, M. Saleem, F. Salemi, A. Samajdar, L. Sammut, L. M. Sampson, E. J. Sanchez, V. Sandberg, B. Sandeen, G. H. Sanders, J. R. Sanders, B. Sassolas, B. S. Sathyaprakash, P. R. Saulson, O. Sauter, R. L. Savage, A. Sawadsky, P. Schale, R. Schilling, J. Schmidt, P. Schmidt, R. Schnabel, R. M. S. Schofield, A. Schönbeck, E. Schreiber, D. Schuette, B. F. Schutz, J. Scott, S. M. Scott, D. Sellers, A. S. Sengupta, D. Sentenac, V. Sequino, A. Sergeev, G. Serna, Y. Setyawati, A. Seigny, D. A. Shaddock, T. Shaffer, S. Shah, M. S. Shahriar, M. Shaltev, Z. Shao, B. Shapiro, P. Shawhan, A. Sheperd, D. H. Shoemaker, D. M. Shoemaker, K. Siellez, X. Siemens, D. Sigg, A. D. Silva, D. Simakov, A. Singer, L. P. Singer, A. Singh, R. Singh, A. Singhal, A. M. Sintes, B. J. J. Slagmolen, J. R. Smith, M. R. Smith, N. D. Smith, R. J. E. Smith, E. J. Son, B. Sorazu, F. Sorrentino, T. Souradeep, A. K. Srivastava, A. Staley, M. Steinke, J. Steinlechner, S. Steinlechner, D. Steinmeyer, B. C. Stephens, S. P. Stevenson, R. Stone, K. A. Strain, N. Straniero, G. Stratta, N. A. Strauss, S. Strigin, R. Sturani, A. L. Stuver, T. Z. Summerscales, L. Sun, P. J. Sutton, B. L. Swinkels, M. J. Szczepańczyk, M. Tacca, D. Talukder, D. B. Tanner, M. Tápai, S. P. Tarabrin, A. Taracchini, R. Taylor, T. Theeg, M. P. Thirugnanasambandam, E. G. Thomas, M. Thomas, P. Thomas, K. A. Thorne, K. S. Thorne, E. Thrane, S. Tiwari, V. Tiwari, K. V. Tokmakov, C. Tomlinson, M. Tonelli, C. V. Torres, C. I. Torrie, D. Töyrä, F. Travasso, G. Traylor, D. Trifirò, M. C. Tringali, L. Trozzo, M. Tse, M. Turconi, D. Tuyenbayev, D. Ugolini, C. S. Unnikrishnan, A. L. Urban, S. A. Usman, H. Vahlbruch, G. Vajente, G. Valdes, M. Vallisneri, N. van Bakel, M. van Beuzekom, J. F. J. van den Brand, C. Van Den Broeck, D. C. Vander-Hyde, L. van der Schaaf, J. V. van Heijningen, A. A. van Veggel, M. Vardaro, S. Vass, M. Vasúth, R. Vaulin, A. Vecchio, G. Vedovato, J. Veitch, P. J. Veitch, K. Venkateswara, D. Verkindt, F. Vetrano, A. Viceré, S. Vinciguerra, D. J. Vine, J.-Y. Vinet, S. Vitale, T. Vo, H. Vocca, C. Vorvick, D. Voss, W. D. Voursden, S. P. Vyatchanin, A. R. Wade, L. E. Wade, M. Wade, S. J. Waldman, M. Walker, L. Wallace, S. Walsh, G. Wang, H. Wang, M. Wang, X. Wang, Y. Wang, H. Ward, R. L. Ward, J. Warner, M. Was, B. Weaver, L.-W. Wei, M. Weinert, A. J. Weinstein, R. Weiss, T. Welborn, L. Wen, P. Weßels, T. Westphal, K. Wette, J. T. Whelan, S. E. Whitcomb, D. J. White, B. F. Whiting, K. Wiesner, C. Wilkinson, P. A. Willems, L. Williams, R. D. Williams, A. R. Williamson, J. L. Willis, B. Willke, M. H. Wimmer, L. Winkelmann, W. Winkler, C. C. Wipf, A. G. Wiseman, H. Wittel, G. Woan, J. Worden, J. L. Wright, G. Wu, J. Yablon, I. Yakushin, W. Yam, H. Yamamoto, C. C. Yancey, M. J. Yap, H. Yu, M. Yvert, A. Zadrożny, L. Zangrando, M. Zanolin, J.-P. Zendri, M. Zevin, F. Zhang, L. Zhang, M. Zhang, Y. Zhang, C. Zhao, M. Zhou,

- Z. Zhou, X. J. Zhu, M. E. Zucker, S. E. Zuraw, and J. Zweizig. Observation of Gravitational Waves from a Binary Black Hole Merger. *Physical Review Letters*, 116(6):061102, February 2016.
- [28] Zin Lin, Xiangdong Liang, Marko Lončar, Steven G. Johnson, and Alejandro W. Rodriguez. Cavity-enhanced second-harmonic generation via nonlinear-overlap optimization. *Optica*, 3(3):233–238, March 2016.
- [29] Joshua McNeur et al. Elements of a dielectric laser accelerator. *arXiv preprint arXiv:1604.07684*, 2016.
- [30] K Mizuno et al. Experimental evidence of the inverse Smith–Purcell effect. *Nature*, 328(6125):45–47, 1987.
- [31] Sean Molesky, Zin Lin, Alexander Y. Piggott, Weiliang Jin, Jelena Vucković, and Alejandro W. Rodriguez. Inverse design in nanophotonics. *Nature Photonics*, 12(11):659, November 2018.
- [32] P Musumeci et al. High energy gain of trapped electrons in a tapered, diffraction-dominated inverse-free-electron laser. *Phys. Rev. Lett.*, 94(15):154801, 2005.
- [33] Jorge Nocedal. Updating quasi-Newton matrices with limited storage. *Math. Comput.*, 35(151):773–782, 1980.
- [34] M. Necat Ozisik. *Inverse Heat Transfer : Fundamentals and Applications*. Routledge, May 2018.
- [35] E. A. Peralta et al. Demonstration of electron acceleration in a laser-driven dielectric microstructure. *Nature*, 503(7474):91–94, 2013.
- [36] Alexander Y. Piggott, Jesse Lu, Konstantinos G. Lagoudakis, Jan Petykiewicz, Thomas M. Babinec, and Jelena Vučković. Inverse design and demonstration of a compact and broadband on-chip wavelength demultiplexer. *Nature Photonics*, 9(6):374–377, June 2015.
- [37] T Plettner and RL Byer. Microstructure-based laser-driven free-electron laser. *Nucl. Instrum. Methods Phys. Res., Sect. A*, 593(1):63–66, 2008.
- [38] T Plettner et al. Proposed few-optical cycle laser-driven particle accelerator structure. *Phys. Rev. ST Accel. Beams*, 9(11):111301, 2006.
- [39] C. R Pollock and Michal Lipson. *Integrated photonics*. Kluwer Academic, Norwell, Mass., 2010. OCLC: 854553854.
- [40] Aaswath P. Raman, Marc Abou Anoma, Linxiao Zhu, Eden Rephaeli, and Shanhui Fan. Passive radiative cooling below ambient air temperature under direct sunlight. *Nature*, 515(7528):540–544, November 2014.



- [41] Wonseok Shin and Shanhui Fan. Choice of the perfectly matched layer boundary condition for frequency-domain Maxwell's equations solvers. *J. Comput. Phys.*, 231(8):3406–3431, 2012.
- [42] Ole Sigmund. Systematic Design of Metamaterials by Topology Optimization. In R. Pyrz and J. C. Rauhe, editors, *IUTAM Symposium on Modelling Nanomaterials and Nanosystems*, IUTAM Bookseries, pages 151–159. Springer Netherlands, 2009.
- [43] Ken Soong et al. Laser damage threshold measurements of optical materials for direct laser accelerators. *AIP Conf. Proc.*, 1507(1):511–515, 2012.
- [44] Allen Taflove and Susan C Hagness. *Computational Electrodynamics: The Finite-Difference Time-Domain Method*. Artech House Publishers, Norwood, MA, 2nd edition, 2000.
- [45] Masataka Tanaka and G. S. Dulikravich. *Inverse Problems in Engineering Mechanics*. Elsevier, November 1998. Google-Books-ID: tyOpk49g0vsC.
- [46] N. H. E. Weste and K. Eshraghian. Principles of CMOS VLSI design: A systems perspective. *NASA STI/Recon Technical Report A*, 85, 1985.
- [47] Darrell Whitley. A genetic algorithm tutorial. *Statistics and Computing*, 4(2):65–85, June 1994.
- [48] Zongfu Yu, Aaswath Raman, and Shanhui Fan. Fundamental limit of nanophotonic light trapping in solar cells. *Proceedings of the National Academy of Sciences*, 107(41):17491–17496, October 2010.
- [49] T B Zhang et al. Stimulated dielectric wake-field accelerator. *Phys. Rev. E*, 56(4):4647, 1997.